

A simple analytical model of the diurnal Ekman layer

Jacob O. Wenegrat * †

*Joint Institute for the Study of the Atmosphere and Ocean, University of Washington, Seattle,
Washington*

Michael J. McPhaden

*Pacific Marine Environmental Laboratory, National Oceanic and Atmospheric Administration,
Seattle, Washington*

*Current Affiliation: Department of Environmental Earth System Science, Stanford University,
Stanford, California

†Corresponding author address: Jacob O. Wenegrat, Department of Environmental Earth System
Science, Stanford University, Stanford, CA 94305.

E-mail: jwenegrat@stanford.edu

ABSTRACT

13 The effects of time-varying turbulent viscosity on horizontal currents in the
14 ocean surface boundary layer are considered using a simple theoretical model
15 that can be solved analytically. This model reproduces major aspects of the
16 near-surface ocean diurnal cycle in velocity and shear, while retaining direct
17 parallels to the steady-state Ekman solution. The parameter dependence of
18 the solution is explored qualitatively, and quantitative measures of the low-
19 frequency rectification of velocity and shear are derived. Results demonstrate
20 that time-variability in eddy viscosity leads to significant changes to the time-
21 averaged velocity and shear fields, with important implications for the in-
22 terpretation of observations, and modeling of the near-surface ocean. These
23 findings mirror those of more complete numerical modeling studies, suggest-
24 ing that some of the rectification mechanisms active in those studies may be
25 independent of the details of the boundary layer turbulence.

26 **1. Introduction**

27 The daily transit of the sun causes a daily cycle in surface heat flux that is a principal forc-
28 ing of upper ocean variability. This diurnal cycle in surface heat flux leads to a diurnal cycle in
29 temperature, stratification, and near-surface mixing (Smyth 1854; Stommel et al. 1969; Brainerd
30 and Gregg 1993). The effects of these changes have been the subject of widespread study in
31 the oceanographic literature, and beyond the purely physical implications, a host of bio-physical
32 interactions on the diurnal scale have been identified (McCreary et al. 2001; Kawai and Wada
33 2007). The effects of the ocean diurnal cycle have also been studied extensively from the atmo-
34 spheric perspective, as diurnal sea-surface temperature variability is critical to atmospheric bound-
35 ary layer moisture content and convection, which respond non-linearly to temperature (Chen and
36 Houze 1997; Clayson and Chen 2002; Dai and Trenberth 2004). The ability of the diurnal cycle
37 in surface heat flux to modify low-frequency ocean temperature variability, a process termed rec-
38 tification, has also been studied in the context of models, where it is shown that diurnal variability
39 modifies the mean state on intraseasonal and longer timescales (Shinoda 2005; Danabasoglu et al.
40 2006; Bernie et al. 2007, 2008).

41 While the ocean thermodynamic response has been the subject of much work, the dynamic re-
42 sponse remains less well understood. Observations have established that diurnal variability in
43 stratification can serve to inhibit turbulent vertical momentum flux, causing the near-surface con-
44 vergence of wind-driven momentum that leads to the acceleration of a downwind diurnal jet (Price
45 et al. 1986). These jets are highly sheared, lowering the flow Richardson number to allow for
46 the development of shear instabilities that deepen the mixed layer before the surface heat flux has
47 changed sign, suggesting the dynamics of the ocean response are intertwined with the thermody-
48 namic response (Smyth et al. 2013; Wenegrat and McPhaden 2015). Diurnal variability of mixing

49 has also been implicated in departures of time-averaged velocity fields from the predictions of
50 classic Ekman theory (Price and Sundermeyer 1999), although the observational evidence alone
51 has not been conclusive in this regards (Lewis and Belcher 2004; Raschle and Arduin 2009).

52 Much of the theoretical work on the dynamics of the ocean diurnal cycle has focused on the use
53 of slab layer models, which while useful in their simplicity, by construction do not offer any insight
54 into the vertical structure of the flow. Further, observations suggest that Ekman theory provides
55 a more consistent description of subinertial variability than slab layer models do (Davis et al.
56 1981; Weller and Plueddemann 1996; Elipot and Gille 2009; Kim et al. 2014), and hence utilizing
57 slab layer physics to understand rectification effects may not be appropriate. Thus, despite the
58 recognized importance of the diurnal cycle, questions remain about the dynamical response to
59 diurnal forcing, in particular regarding the possible routes to dynamical rectification.

60 Important work on this topic was undertaken by McWilliams and Huckle (2006), and
61 McWilliams et al. (2009), in the context of idealized numerical models. They showed that transient
62 winds, surface buoyancy fluxes, and interior eddy fluxes result in rectification to the time-mean
63 flow, attributed principally to modifications of the turbulent boundary layer depth and nonlinear-
64 ities in the parameterized eddy viscosity (McWilliams and Huckle 2006; McWilliams et al. 2009).
65 These findings are significant contributions to our understanding of dynamical rectification ef-
66 fects, particularly in their ability to elucidate the terms controlling changes in turbulent mixing
67 under different forcing regimes. However, as is often the case, the greater physical realism en-
68 abled by a numerical model comes at the expense of additional complexity, and thus the parameter
69 dependence and underlying physics are not as clearly illuminated as with theoretical approaches.

70 Here we take a simpler approach, situated in complexity between analytic slab layer models and
71 more realistic numerical models, and consider a periodic solution for the time-dependent Ekman
72 layer (section 2). The eddy viscosity is treated as an external parameter, allowed to vary sinu-

73 soidally in time to approximate the known time-variability of turbulent mixing. This approach
74 excludes any feedbacks between the wind-driven shear and the eddy viscosity, which is at best a
75 crude first-order approximation (cf. McWilliams et al. 2009). However, the ability of the result-
76 ing model to reproduce major aspects of the diurnal cycle in the near-surface ocean, as well its
77 analytic tractability and possibility for insight into the underlying physical processes, particularly
78 dynamical rectification, suggest it is a worthwhile exercise (section 3). In this respect, aspects
79 of this work are similar to approaches used extensively in the study of the dynamics of low-level
80 jets in the atmospheric boundary layer (Buajitti and Blackadar 1957; Singh et al. 1993; Tan and
81 Farahani 1998; Zhang and Tan 2002), which to our knowledge have not yet been applied to the
82 oceanographic problem.

83 2. Theory

84 We consider a linearized model of time-dependent horizontal flow, written using complex nota-
85 tion as $\vec{u} = u + iv$. The horizontal momentum equations are thus given by,

$$\vec{u}_t + if\vec{u} = -\frac{1}{\rho}\nabla p + (A_v(z,t)\vec{u}_z)_z, \quad (1)$$

86 with subscript t , and z , denoting differentiation with respect to time and the vertical coordinate,
87 respectively. The eddy viscosity is denoted as A_v , and the density by ρ . It is assumed that the
88 horizontal pressure gradient, ∇p , is independent of z , allowing separation into geostrophic and
89 ageostrophic components, although we caution that baroclinic pressure gradients can be expected
90 to significantly modify ageostrophic flows in the real ocean (Wenegrat and McPhaden 2016). The
91 focus of this work is on the wind-driven flow, hence for the remainder we set $\nabla p = 0$. We thus
92 seek a solution to,

$$\vec{u}_t + if\vec{u} = (A_v(z,t)\vec{u}_z)_z. \quad (2)$$

93 Transforming $\vec{u} = e^{-if t} \vec{w}$ reduces (2) to the one-dimensional heat equation with a coefficient that
 94 varies in both time and space,

$$\vec{w}_t = (A_v(z, t) \vec{w}_z)_z. \quad (3)$$

95 Similar equations arise in the study of a variety of physical phenomenon, including non-Newtonian
 96 fluids (Balmforth and Craster 2001), diffusion in porous materials such as concrete (Mangat and
 97 Molloy 1994), and heat conduction in radioactive materials (Cannon 1984). For vertically uniform
 98 A_v , with arbitrary time dependence, it is possible to find a unique transformation of the time co-
 99 ordinate such that the solution can be written as a convolution between a transfer function and the
 100 time-varying surface wind stress (cf. Cannon 1984, 13.1.1-13.1.8). An example integral solution
 101 for an impulsively started steady wind stress, $\vec{\tau}$, was given by Csanady and Shaw (1980),

$$\vec{u}(z, t) = \frac{\vec{\tau}}{\rho} \int_0^t \frac{e^{-if(t-\eta)}}{\sqrt{\pi Q(\eta)}} e^{-\frac{z^2}{4Q(\eta)}} d\eta, \quad (4)$$

$$Q(y) = \int_{t-y}^t A_v(T) dT. \quad (5)$$

103 This solution was considered further, and extended to time-varying wind stress, in Wenegrat
 104 (2015), where it was found that monochromatic periodic time-variability in A_v introduces a com-
 105 plex modulation of the ocean velocity field at all frequencies. Here we take advantage of the
 106 existence of an oscillatory steady-state solution for the case of steady wind stress, that was evident
 107 in this earlier work (Wenegrat 2015), to provide a simple time-periodic solution for the case of
 108 steady-wind forcing and periodically varying $A_v(z, t)$.

109 We thus seek solutions of (2), subject to the following conditions,

$$\vec{u}(z, t) = \vec{u}(z, t + \frac{2\pi}{\omega}), \quad (6a)$$

$$\vec{u}_z(0, t) = \frac{\vec{\tau}_w}{\rho A_v(0, t)}, \quad (6b)$$

$$\vec{u} \rightarrow 0, \quad z \rightarrow -\infty. \quad (6c)$$

110 Equation (6a) expresses the periodic-time boundary condition, with frequency ω . For the mo-
 111 tivating reasons given in section 1, we will identify this with the diurnal frequency, although
 112 the solution is valid generally for any ω . The surface boundary condition, (6b), is the standard
 113 shear-stress boundary condition where the wind stress is assumed constant in time, and the eddy
 114 viscosity is allowed to be a function of both time and space, $A_v(z, t)$. The results discussed here
 115 are not sensitive to the particular bottom boundary condition, hence for simplicity we use, (6c),
 116 the standard Ekman bottom boundary condition. The derivation given can easily be applied to
 117 alternate boundary conditions.

118 $A_v(z, t)$ is assumed to be a known parameter, and we require that it be separable in time and
 119 space, $A_v(z, t) = A(z)K(t)$. The dimensional vertical structure, $A(z)$, can take any form that satis-
 120 fies the requirements of a Wentzel-Kramers-Brillouin-Jeffreys approximation (WKBJ, Bender and
 121 Orszag 1978), discussed below. However, we require that the time dependence take a particular
 122 form (Buajitti and Blackadar 1957),

$$K(t) = 1 + \delta \cos(\omega t), \quad (7)$$

123 with $\delta \in [0, 1)$, determining the strength of the periodic cycle of mixing. These mathematically ex-
 124 pedient requirements on A_v are not expected to accurately reflect the diurnal cycle of near-surface
 125 mixing, which remains an active area of observational work. Notably, parameterizations based on
 126 similarity theory with time varying boundary layer depth, such as the K-Profile Parameterization
 127 (KPP, Large et al. 1994), result in A_v where space-time dependence is not formally separable,
 128 discussed further in Appendix A.

129 However, the idealized form of A_v we use here can be justified in part based on observations of
 130 the diurnal cycle of near-surface A_v which suggests that a sinusoidal time dependence is a reason-
 131 able first approximation (Wenegrat and McPhaden 2015). An example composite diurnal cycle,

132 estimated indirectly from ~ 3 months of moored observations of wind-stress and near-surface ve-
 133 locity, following the method given in Wenegrat et al. (2014), is shown in figure 1, demonstrating
 134 the essentially sinusoidal time-dependence. Further support for this idealized time-dependence of
 135 A_V comes from a posteriori comparisons of the theory with more complete numerical models (sec-
 136 tion 3a, and Appendix A). Note also that the periodic time-variability in (7) introduces no change
 137 to the diurnally averaged A_V , which facilitates comparison to the steady ($\delta = 0$) solution.

138 We can rewrite equation (3) as,

$$\vec{w}_t(z, t) = K(t)[A(z)\vec{w}(z, t)]_z. \quad (8)$$

139 Transforming the time coordinate, such that $\zeta = t + \delta/\omega \sin(\omega t)$, gives,

$$\vec{w}_\zeta = [A(z)\vec{w}_z]_z. \quad (9)$$

140 In the new coordinate system the time periodic condition, (6a), can be written as, $\vec{w}(z, \zeta + \frac{2\pi}{\omega}) =$
 141 $\vec{w}(z, \zeta)e^{if\frac{2\pi}{\omega}}$ (Zhang and Tan 2002), which is true of,

$$\vec{w}(z, \zeta) = \vec{W} \sum_{n=-\infty}^{\infty} \vec{w}_n(z)e^{i(f+n\omega)\zeta}. \quad (10)$$

142 Substituting (10) into (9) gives a series of ordinary differential equations,

$$[A(z)(\vec{w}_n)_z]_z - i(f + n\omega)\vec{w}_n = 0, \quad (11)$$

143 which are equivalent to those studied by Zhang and Tan (2002).

144 Each of the n-equations defined by equation (11) are straightforward to solve numerically, or, for
 145 additional insight into the dynamics, the solutions can be approximated using the WKBJ method
 146 (Grisogono 1995), which assumes,

$$w_n \propto e^{\frac{1}{\epsilon_n}(S_0 + \epsilon_n S_1 + \epsilon_n^2 S_2 \dots)}. \quad (12)$$

147 Non-dimensionalizing in the standard manner for the Ekman balance (e.g. Vallis 2006, section
 148 2.12.1) with a modified rotational frequency of $f + n\omega$ gives,

$$Ek_n [\hat{A}(z)(\hat{w}_n)_{\hat{z}\hat{z}} + \hat{A}(z)_{\hat{z}}\hat{w}_n] - i\hat{w} = 0, \quad (13)$$

149 where the hat notation indicates non-dimensional quantities, $Ek_n = \frac{A_0}{(f+n\omega)D^2}$ is the mode Ekman
 150 number, and A_0 is a representative scale value of A_v . We identify D with the depth scale over which
 151 $A(z)$ varies, as per the discussion in Wenegrat and McPhaden (2016). Ek_n thus characterizes the
 152 ratio of the depth scale of the n^{th} mode boundary layer to the depth scale over which $A(z)$ varies.
 153 Using (12) in (13) gives $\varepsilon_n \sim Ek_n^{\frac{1}{2}}$, and the WKBJ balance equations,

$$S_0 = \sqrt{i} \int_z^0 \hat{A}(Z)^{-\frac{1}{2}} dZ, \quad (14)$$

$$S_1 = -\frac{1}{4} \log \hat{A}(z). \quad (15)$$

155 Use of the WKBJ approximation requires that,

$$\frac{Ek_n^{\frac{1}{2}} S_1}{S_0} \ll 1, \quad Ek_n^{\frac{1}{2}} \rightarrow 0, \quad (16)$$

$$Ek_n^{\frac{1}{2}} S_2 \ll 1, \quad Ek_n^{\frac{1}{2}} \rightarrow 0, \quad (17)$$

157 which physically can be understood as requiring slow variation of A_v relative to the boundary layer
 158 thickness of the n^{th} mode. The constraint this places on the validity of the WKBJ approximation
 159 will be strongest for the $n = 0$ mode, as higher modes become rapidly surface trapped. A specific
 160 case where this WKBJ expansion is formally incorrect is the case of $f = \pm n\omega$, where mode $\mp n$
 161 will have $Ek_n \rightarrow \infty$. However, these modes are zeros of the Bessel functions used in the solutions
 162 below, so do not contribute appreciably to the total solution, discussed in more detail in Appendix
 163 **B**.

164 To simplify the analysis, we consider only simple profiles of $A(z)$ which stay sufficiently large
 165 so as to not violate (16), which precludes the direct application of this approximation to many

166 common forms of parameterized A_v (O'Brien 1970; Large et al. 1994). If desired, this require-
 167 ment can be removed by patching an appropriate inner solution as in Wenegrat and McPhaden
 168 (2016). However, as discussed below, many of the results emphasized here are independent of the
 169 particular form of $A(v)$.

170 The solution for an arbitrary mode after application of the bottom boundary condition is thus,

$$w_n(z) = C_n A(z)^{-\frac{1}{4}} e^{-(1+i) \int_z^0 h_{Ek_n}^{-1}(Z) dZ}, \quad (18)$$

171 such that h_{Ek_n} defines the mode's depth dependent Ekman depth, $h_{Ek_n}(z) = \sqrt{2A(z)/(f+n\omega)}$.

172 The surface boundary condition, (6b), can be considered by returning to the series expansion
 173 (10), in terms of $w_z(z, \zeta)$,

$$\sum_{n=-\infty}^{\infty} C_n \frac{\sqrt{2i} \chi_n(0) h_{Ek_0}(0)}{A(0)^{\frac{1}{4}} h_{Ek_n}(0)} e^{[i(f+n\omega)\zeta]} = \frac{e^{ift(\zeta)}}{K(t(\zeta))}, \quad (19)$$

174 where we have set $\vec{W} = \vec{\tau}_w h_{Ek_0}(0) (A(0)\rho)^{-1}$, and,

$$\chi_n(z) = 1 - \frac{\sqrt{-2i} A(z)_z}{8 A(z)} h_{Ek_n}(z). \quad (20)$$

175 Transforming back to the original time coordinate, writing equation (7) as $K(t) = 1 + \delta/2(e^{i\omega t} +$
 176 $e^{-i\omega t})$, and dividing equation (19) through by the right-hand side gives,

$$\sum_{n=-\infty}^{\infty} C_n \frac{\sqrt{2i} \chi_n(0) h_{Ek_0}(0)}{A(0)^{\frac{1}{4}} h_{Ek_n}(0)} \left[e^{in\omega t + i\delta(\frac{f}{\omega} + n)\sin(\omega t)} + \frac{\delta}{2} e^{i(n+1)\omega t + i\delta(\frac{f}{\omega} + n)\sin(\omega t)} + \frac{\delta}{2} e^{i(n-1)\omega t + i\delta(\frac{f}{\omega} + n)\sin(\omega t)} \right] = 1 \quad (21)$$

177 Note that if integrated in time each of the exponential terms takes the form of a Bessel function of
 178 the first kind (Temme 1996; Zhang and Tan 2002), thus,

$$\sum_{n=-\infty}^{\infty} (-1)^n C_n \frac{\sqrt{2i} \chi_n(0) h_{Ek_0}(0)}{A(0)^{\frac{1}{4}} h_{Ek_n}(0)} \left[J_n(\delta(\frac{f}{\omega} + n)) - \frac{\delta}{2} J_{n+1}(\delta(\frac{f}{\omega} + n)) - \frac{\delta}{2} J_{n-1}(\delta(\frac{f}{\omega} + n)) \right] = 1, \quad (22)$$

179 where J_n denotes the n^{th} Bessel function of the first kind (Temme 1996). The surface boundary
 180 condition is therefore satisfied if,

$$C_n = (-1)^n \sqrt{-2i} J_n \left(\delta \left(\frac{f}{\omega} + n \right) \right) \frac{A(0)^{\frac{1}{4}} h_{Ek_n}(0)}{2\chi_n(0) h_{Ek_0}(0)}. \quad (23)$$

181 For simplicity in presentation we assume that $A(z)$ does not vary significantly at $z = 0$ relative
 182 to the mode Ekman depth, ie. $\chi_n(0) \sim 1$, although we retain this factor in subsequent calculations.

183 The full solution is therefore given by,

$$\vec{u}(z, t) = \frac{\vec{\tau}_w}{\rho \sqrt{fA(0)}} e^{-i\frac{\pi}{4}} \sum_{n=-\infty}^{\infty} \left[\underbrace{(-1)^n \left(\frac{f}{f+n\omega} \right)^{1/2}}_{\text{I}} J_n(\gamma_n) \underbrace{\Omega_n(z)}_{\text{II}} \underbrace{e^{i(n\omega t + \gamma_n \sin(\omega t))}}_{\text{III}} \right], \quad (24a)$$

184 where

$$\Omega_n(z) = \left(\frac{A(0)}{A(z)} \right)^{\frac{1}{4}} e^{-(1+i) \int_z^0 h_{Ek_n}^{-1}(Z) dZ}, \quad (24b)$$

$$\gamma_n = \delta \left(\frac{f}{\omega} + n \right). \quad (24c)$$

185 Note that only the vertical structure functions (24b) are approximate, and in the case that A_V is
 186 vertically uniform this solution is exact.

187 The term outside the summation defines the standard Ekman velocity scale, as arises in the
 188 steady-state problem. This amplitude term then multiplies an infinite series of oscillating vertical
 189 modes, each with vertical structure determined by the boundary layer ordinary differential equation
 190 (11). Term II (equation 24b) defines the vertical structure of the individual modes, each of which is
 191 a solution to a steady-state Ekman problem with a modified rotational frequency of $f + n\omega$. Thus,
 192 higher modes are progressively more surface trapped, with boundary layer depth scale h_{Ek_n} . The
 193 extent of the vertical trapping of higher modes can be noted by considering that for the diurnal
 194 period considered here, mode $n = 2$ has a vertical depth scale less than that of a traditional Ekman
 195 layer at latitude 90° . It can be anticipated from this that, in the time-periodic problem, oscillating
 196 A_V leads to a shoaling of the mean flow relative to the constant A_V solution (section 3c).

197 The value of the full summation in equation (24a) at $z = 0$ is determined by the surface boundary
 198 condition, equation (6b), however, for a given value of δ some modes will be excited more than
 199 others. Term I of (24a) thus can be considered as determining how efficiently the wind stress
 200 projects onto each mode, with larger values of δ leading to more significant excitation of higher
 201 modes (figure 2). The ratio f/ω in γ determines the symmetry of modes that are excited, with
 202 $f/\omega \rightarrow 0$ leading to a symmetric excitation of positive and negative modes, whereas larger values
 203 of f/ω are skewed towards positive modes (figure 2). When $\delta = 0$, $J_0(0) = 1$ and $J_n(0) = 0$ for
 204 $n \neq 0$, such that only the zeroth Bessel function is excited, and the steady state Ekman solution is
 205 recovered.

206 The time-dependence in (24a) is a complex modulated oscillation (figure 3). Mathematically
 207 the time-dependence of each mode takes the form of a frequency-modulated signal, oscillating at
 208 frequency ω , with carrier frequency $n\omega$. This similarity can be exploited to rewrite (24a) with a
 209 simpler time-dependence, at the expense of a more complex expression for the mode amplitude
 210 and depth dependence,

$$\vec{u}(z,t) = \frac{\vec{\tau}_w}{\rho \sqrt{fA(0)}} e^{-i\frac{\pi}{4}} \sum_{l=-\infty}^{\infty} \left[\sum_{n=-\infty}^{\infty} (-1)^n \left(\frac{f}{f+n\omega} \right)^{1/2} J_n(\gamma_n) J_{l-n}(\gamma_n) \Omega_n(z) \right] e^{il\omega t}. \quad (25)$$

211 3. Discussion of Solution

212 In this section several pertinent aspects of the solution (24a) will be explored, including a quan-
 213 titative formulation of the rectification of velocity and shear in the time-averaged solution.

214 a. Qualitative Solution Characteristics

215 Figure 4 shows an example solution hodograph, where it assumed that A_v is elevated between
 216 1800 – 0600 hours, with the daily minimum occurring at 1200 hours. Velocity vectors trace closed
 217 contours over a 24 hour period, the time average of which is shown (heavy black), and which

218 can be compared to the steady-state Ekman solution (dashed black). Differences between these
219 lines represent rectification of the diurnal variability in A_v to the low-frequency velocity field.
220 Understanding and quantifying these rectification effects is the focus of section 3c below.

221 Further insight into the solution comes from considering the solution in the time-depth plane.
222 Figure 5 shows an example solution for a mid-latitude Ekman layer forced by a constant zonal
223 wind stress. In the early morning hours A_v is high, and the Ekman layer is at its deepest. As A_v
224 decreases towards its mid-day minimum the Ekman layer begins to shoal, most clearly evident in
225 the shoaling of the zero zonal velocity line from $z \sim -1h_{Ek_0}$ to $z \sim -0.5h_{Ek_0}$. A surface intensified
226 diurnal jet develops (Price et al. 1986), associated with a high shear near surface layer. Below this
227 high shear region, weak anticyclonic oscillations, with upward propagating phase, begin. In the
228 near-surface ocean, near-inertial variability with upward propagating phase is often attributed to
229 inertial waves with downward energy propagation. However the one-dimensional nature of the
230 solution considered here precludes the existence of internal waves. Instead these features should
231 be interpreted as inertial oscillations, with phase propagation determined by the diurnal cycle in
232 viscosity, as discussed further below.

233 The primary zonal momentum balance throughout the diurnal evolution is between the Coriolis
234 acceleration, $-fv$, and the turbulent momentum flux convergence, $(A_v u_z)_z$, consistent with Ekman
235 layer dynamics (figure 6). Near-the surface there is an alternating acceleration and deceleration
236 of the flow on either side of the diurnal jet maximum, necessary to maintain the classic Ekman
237 transport as the Ekman depth shoals and deepens. Deeper in the layer there are upward propa-
238 gating signals in acceleration that are balanced largely by the Coriolis acceleration, a signature of
239 inertial oscillations. These features can thus be interpreted as inertial oscillations initiated by the
240 loss of Ekman balance caused by the decreasing mid-day A_v . In this manner they are similar to
241 the inertial oscillations observed in simple models of the nocturnal low-level jet in the atmospheric

242 boundary layer, where it is found that a layer which abruptly transitions from viscous to inviscid
243 dynamics, representing the change between daytime and nighttime dynamics, causes inertial os-
244 cillations around the equilibrium solution (Blackadar 1957; Van de Wiel et al. 2010). The model
245 considered here is not completely inviscid at depth, but, by analogy with atmospheric low level
246 jets, leads to inertial oscillations which progressively shoal, following the shoaling Ekman layer.

247 Figure 7 compares a more realistic simulation from a 1D model forced by a diurnal cycle in
248 surface buoyancy fluxes (Appendix A), utilizing the KPP turbulence parameterization (Large et al.
249 1994). The right panels show the time-periodic theoretical solution, forced by the same surface
250 wind stress, using values of A_V diagnosed from the numerical model output. The boundary value
251 problems, equation (11), are solved numerically for simplicity and accuracy, rather than using
252 the WKBJ approximation (see Wenegrat and McPhaden 2016, for a discussion of the use of the
253 WKBJ approximation for $A_V(z)$ based on similarity theory). Major features are well reproduced,
254 including the near-surface diurnal jet, mid depth minima in zonal velocity, descending shear layers,
255 suppressed nighttime shear, and enhancement of shear near the base of the turbulent boundary
256 layer. Other features which are not well reproduced are the stronger inertial oscillations below the
257 boundary layer evident in the numerical model, and the deep evolution of the descending diurnal
258 shear layers, whose descent slows in the numerical model relative to the theoretical prediction.
259 These features are likely attributable in part to the lack of internal wave radiation in the 1D model
260 configuration, and the space-time coupling of turbulent viscosity in KPP, respectively.

261 *b. Parameter Dependence*

262 In this section the parameter dependence of the solution (24a) will be explored to illustrate how
263 the dynamics evolve across different regimes. The aspects of the solution unique to the diurnal
264 cycle are evidently controlled by only two non-dimensional parameters, δ the strength of the

265 diurnal A_V cycle (equation (7)), and f/ω , the ratio between the local inertial frequency and the
266 period of the eddy viscosity. Figure 8 illustrates the modification of boundary layer currents as
267 δ is varied. Increasing δ increases the strength of the near-surface diurnal jet, as expected from
268 the momentum balance discussed above. The strength, and location, of the inertial oscillations are
269 also affected, with increasing δ leading to higher velocities, occurring closer to the surface and
270 slightly later in the day. Similarly, with higher δ the enhanced near-surface shear persists later in
271 the day, with evident subsurface maxima occurring several hours after the daily minimum in A_V .

272 Figure 9 compares the effect of varying latitude, holding δ constant. At low latitudes an af-
273 ternoon deepening of the sheared diurnal jet is evident, whereas the near-surface velocity and
274 shear response becomes increasingly symmetric around the mid-day minimum in A_V as latitude
275 increases. Deeper in the layer, $z \sim -4h_{Ek_0}$, the diurnal modulation becomes increasingly pro-
276 nounced as latitude increases. An upward propagating inertial oscillation is only clearly evident
277 for 45° , which may result from the inability of the periodic domain considered here to support
278 inertial oscillations for latitudes $< 30^\circ$, where the inertial period exceeds 1 day. These effects
279 are a consequence purely of varying latitude, while holding A_V fixed, and are therefore separate
280 from those arising due to the horizontal component of the Coriolis force, which has been shown to
281 modify boundary layer flow through altering the turbulence intensity and Reynolds stress (Zikanov
282 et al. 2003; McWilliams and Huckle 2006).

283 The diurnal evolution is also affected by the vertical structure of A_V , as illustrated by a compari-
284 son between the solution for a vertically uniform A_V profile and a more realistic modified Gaussian
285 profile (figure 10). The basic Ekman layer structure is stretched vertically according to the vertical
286 structure of A_V , consistent with the interpretation of the integral in equation (24b) as a stretching of
287 the vertical coordinate based on a vertically localized Ekman depth, as discussed in Wenegrat and
288 McPhaden (2016). This leads to an enhancement of shear in the near-surface, as well as deeper in

289 the layer ($z < -0.5h_{Ek}$), for the modified Gaussian profile, which has reduced A_V in these depth
 290 ranges. Near $z = -0.25h_{Ek}$ the isolines of velocity undergo more pronounced diurnal oscillations
 291 for the modified Gaussian profile, following the discussion in section 3a (figure 6), where it is
 292 suggested that inertial oscillations are generated following the shoaling of the Ekman layer, with
 293 vertical phase speed determined by $\partial h_{Ek}(z)/\partial t$, which for a given value of δ will be enhanced for
 294 larger values of A_V .

295 *c. Rectification*

296 Diurnal variability poses a challenge for the interpretation of observational data in terms of
 297 Ekman dynamics, as observations are frequently averaged in time in order to improve the signal-
 298 to-noise ratio and remove other forms of variability. Understanding the effect of time variability
 299 in A_V is thus critical to understanding time-averaged observations. Integrating the time-dependent
 300 solution (24a) over one diurnal cycle allows for comparison with the steady state solution ($\delta = 0$),
 301 which can be used to examine the rectification effects of the diurnal cycle in mixing. We define a
 302 diurnal average of a quantity $X(t)$ as,

$$\langle X \rangle = \frac{\omega}{2\pi} \int_0^{2\pi/\omega} X(t) dt. \quad (26)$$

303 The solution for velocity averaged over one diurnal cycle is given by,

$$\langle \vec{u}(z) \rangle = \frac{\vec{\tau}_w}{\rho \sqrt{fA(0)}} e^{-i\pi/4} \sum_{n=-\infty}^{\infty} \left[\left(\frac{f}{f+n\omega} \right)^{1/2} J_n^2(\gamma_n) \Omega_n(z) \right]. \quad (27)$$

304 This takes on a particularly simple form at the surface where,

$$\langle \vec{u}(0) \rangle = \frac{\vec{\tau}_w}{\rho \sqrt{fA(0)}} e^{-i\pi/4} \sum_{n=-\infty}^{\infty} \left[\left(\frac{f}{f+n\omega} \right)^{1/2} J_n^2(\gamma_n) \right]. \quad (28)$$

305 As discussed above, the projection coefficients decrease quickly with increasing mode number due
 306 to the rapid roll off of the squared Bessel functions, J_n^2 , and the dependence on $(f/(f+n\omega))^{1/2}$,

307 which is small for large absolute values of n . Thus, the time average solution for velocity will be
308 dominated by the low modes.

309 It is worth noting that the summation in equation (28) can have an imaginary component, arising
310 from modes where $(f + n\omega) < 0$. This can lead to a rotation of the surface velocity relative to the
311 45° deflection predicted by steady-state Ekman theory, as shown in figure 11 as a function of the
312 controlling parameters. Modifications to the direction of the surface current resulting from diurnal
313 variability in A_v are generally quite small ($< 10^\circ$), in the downwind direction, and are hence
314 not likely to be a significant factor in explaining discrepancies between observed surface current
315 deflections and the predictions of classic Ekman theory (Huang 1979). This effect, arising solely
316 from temporal variability in A_v , is however distinct from the changes in the direction of wind-
317 driven flow that result from vertical structure in A_v , through equation (20), which can introduce
318 significant changes in the direction of the ageostrophic flow.

319 In a similar manner, the solution for surface shear averaged over one diurnal cycle can be found
320 by vertically differentiating (27) and evaluating at $z = 0$,

$$\langle \vec{u}_z(0) \rangle = \frac{\vec{\tau}_w}{\rho A(0)} \sum_{n=-\infty}^{\infty} J_n(\gamma_n)^2. \quad (29)$$

321 The higher modes will contribute more to the time average shear solution than they do to the
322 time-averaged velocity, which will lead to larger rectification effects, emphasizing how surface
323 velocity and shear will have different responses to a diurnal cycle in turbulent mixing, a result
324 which is independent of the vertical structure of A_v . Further, the quantity in the summation is
325 positive definite, hence rectification of diurnal variability will always enhance the mean surface
326 shear relative to the steady-state Ekman problem, indicating a shoaling of the mean wind-driven
327 flow.

328 A simple normalized measure of rectification, for a variable X , can be defined as,

$$\hat{X}_R = \frac{||\langle X \rangle| - |\bar{X}||}{|\bar{X}|}, \quad (30)$$

329 where angle brackets as before represent averaging over the diurnal cycle and the bar notation
 330 represents the steady state solution, assuming no time variability in A_V ($\delta = 0$). This measure of
 331 rectification, (30), can then be applied to modeled and theoretical values of velocity and shear to
 332 assess the degree of rectification, giving,

$$\hat{u}_R|_{z=0} = \left| 1 - \sum_{n=-\infty}^{\infty} \left[\left(\frac{f}{f + n\omega} \right)^{1/2} J_n^2(\gamma_n) \right] \right|, \quad (31)$$

333 and,

$$\hat{u}_{zR}|_{z=0} = \left| 1 - \sum_{n=-\infty}^{\infty} J_n(\gamma_n)^2 \right|, \quad (32)$$

334 as shown in figure 12. Velocity rectification increases with increasing δ , with reduced rectification
 335 effects at low-latitudes, due in part to the enhanced total velocities in the Ekman solution as $f \rightarrow 0$.
 336 Shear rectification is essentially latitude independent, which can be anticipated from (32), with a
 337 rapid increase at high δ and maximum values of $\hat{u}_{zR} > 5$ as $\delta \rightarrow 1$. Thus while both velocity and
 338 shear are subject to rectification effects at all latitudes, the vertical structure of the time-averaged
 339 currents are more sensitive than their magnitude to time-variability in A_V .

340 As a basic confirmation of this parameter dependence we compare the approximate theory to a
 341 numerical solution which does not impose the same constraints on periodicity. To do this we nu-
 342 merically solve (2), for an initially motionless ocean forced by a constant zonal wind stress, with a
 343 sinusoidally varying A_V , using a finite element Galerkin method (Skeel and Berzins 1990). Model
 344 integrations are carried out for 50 days, and averages are taken over the last half of the integration.
 345 Rectification in this idealized model can be seen to follow closely to the theoretical prediction
 346 (figure 13). This result holds regardless of latitude, suggesting the time-periodic domain is not

347 unduly influencing this result. Comparisons to a more complete numerical model are presented in
 348 Appendix A.

349 One additional consequence of the changes in the time-mean solution introduced by time-
 350 variability in A_V is that the time-mean current no longer directly satisfies a steady state Ekman
 351 solution. It can thus be anticipated that in order to effectively fit a steady Ekman layer solution to
 352 the resulting currents it will be necessary to define an ‘effective’ A_V which may differ significantly
 353 from the mean of the time-varying values, a result familiar from previous work on Ekman layer
 354 rectification (McWilliams et al. 2009).

355 Following McWilliams et al. (2009, equations 19-21) we define a complex, depth-dependent,
 356 effective eddy viscosity \vec{A}_{vEff} that fits the time-averaged diurnal solution to a steady-state Ekman
 357 model. Namely,

$$\vec{A}_{vEff}(z) = \frac{\int_{-\infty}^z if\langle\vec{u}\rangle dz}{\langle\vec{u}\rangle_z}, \quad (33)$$

358 such that,

$$if\langle\vec{u}\rangle = \left(\vec{A}_{vEff}(z)\langle\vec{u}\rangle_z\right)_z. \quad (34)$$

359 This is shown for a diurnal cycle of A_V that is uniform in depth, which more clearly illustrates
 360 the modifications arising solely from diurnal variability (figure 14). The diurnal cycle of A_V leads
 361 to a reduction in near-surface $|\vec{A}_{vEff}|$, necessary to generate the enhanced near-surface shears. In
 362 all cases there is a mid-depth maximum of $|\vec{A}_{vEff}|$ which moves deeper for increasing values of
 363 δ (off vertical scale for $\delta \geq 0.75$). Positive rotation angles of the effective viscosity indicates
 364 that the diurnally averaged stress is rotated cyclonically relative to the local mean shear, consis-
 365 tent with observations (Price and Sundermeyer 1999; Lenn and Chereskin 2009), and numerical
 366 models (McWilliams et al. 2009). These results can be compared to those from McWilliams et al.

367 (2009, their figure 20) which follow a similar overall structure, suggesting that the rectification
368 mechanisms captured here are relevant to the more complete model physics considered therein.

369 **4. Summary**

370 In this work we have presented a simple theoretical model of the time-dependent Ekman layer
371 with time-periodic eddy viscosity, intended as a basic approximation of the complex and interde-
372 pendent processes governing the real evolution of the ocean surface boundary layer under time-
373 varying forcing (section 2). This model has the advantage of simplicity, illustrating the basic
374 physics of how time-variability in mixing changes the ocean response to a surface wind stress
375 (section 3), and rectifies to the time-mean solution (section 3c). This simplicity comes at the
376 trade-off of physical realism, particularly so in the constraints placed on the vertical and temporal
377 structure of eddy viscosity, and that the turbulent viscosity is not allowed to evolve as a function
378 of the resulting near-surface shear flows. The utility of this model can thus be viewed principally
379 as a means of building physical insight and isolating processes which do not rely on these feed-
380 back mechanisms to occur, as for instance is discussed in regards to the time-mean effective eddy
381 viscosity found in section 3c. It can thus be considered similar to approaches adopted in the atmo-
382 spheric sciences literature on the dynamics of nocturnal low-level jets (Blackadar 1957; Buajitti
383 and Blackadar 1957; Sheih 1972).

384 As guidance for the interpretation of observations, several conclusions can be drawn directly
385 from the work presented here. The discussion of section 2 hints at the complexity of trying to
386 infer the true A_V from measurements of interior velocities or boundary flux values (Wenegrat et al.
387 2014), which in general will require solution of a non-linear equation (cf. Cannon 1984). This is
388 the subject of a large body of literature on inversion techniques for the one-dimensional heat equa-
389 tion which have not been systematically applied to the oceanic problem. The common approach

390 of fitting steady-state Ekman models to time-averaged fields can be expected to result in values of
391 A_V , possibly complex, which depart significantly from the true values, complicating their physical
392 interpretation and limiting their utility. This follows directly from changes in the mean verti-
393 cal structure of the time-dependent solution, without requiring any feedback mechanism between
394 shear flow and A_V , providing a simple explanation of observations (Price and Sundermeyer 1999;
395 Lenn and Chereskin 2009), that differs somewhat in interpretation from previous investigations
396 (McWilliams et al. 2009).

397 Time-variability in A_V modifies both the velocity and vertical structure of ocean currents, and
398 these changes rectify to the low-frequency flow. Velocity shear is more strongly rectified than ve-
399 locity, and in both cases the magnitude of the rectification is only weakly dependent on latitude and
400 dominated by the strength of the periodic variations in mixing. The Ekman solution is non-linearly
401 dependent on A_V , and as demonstrated here, even periodic time variations in A_V , which introduce
402 no change to the time-mean value, can greatly modify the mean boundary layer flow. Finally, we
403 note that the upward propagating inertial oscillations which appear in our solution (figure 6) are
404 forced by the diurnal cycle in viscosity, with vertical phase propagation speed determined by the
405 rate at which the diffusive boundary layer shoals. The dynamics of these oscillations are exactly
406 those implicated in the creation of atmospheric nocturnal jets (Van de Wiel et al. 2010), and im-
407 portantly represent a physical mechanism by which a steady wind-stress forcing, in the presence
408 of a time-varying solar heat flux, can excite near-inertial motions. However their presence in the
409 oceanic boundary layer is less clearly documented, and hence deserves further investigation.

410 *Acknowledgments.* J.O.W. thanks Ren-Chieh Lien and Stephen C. Riser for helpful comments on
411 an earlier version of this manuscript, and two anonymous reviewers for their comments. PIRATA
412 mooring data is available through <http://www.pmel.noaa.gov/tao/>. This publication is partially

413 funded by the Joint Institute for the Study of the Atmosphere and Ocean (JISAO) under NOAA
414 Cooperative Agreement No. NA15OAR4320063, Contribution No. 2495. PMEL contribution
415 4418.

416 APPENDIX A

417 Numerical Model

418 In addition to the basic numerical solution discussed in section 3c, we utilize the MITgcm (Mar-
419 shall et al. 1997), run in an idealized one-dimensional configuration with 2 m vertical resolution,
420 spanning from $z = -500$ to $z = 0$. This resolution is sufficient to resolve the Ekman layer in
421 all simulations used. The model is initiated from a state of rest with a weak, vertically uniform,
422 temperature stratification, equivalent to $N^2 = 2 \times 10^{-5} \text{ s}^{-2}$ ($T_z = 0.01 \text{ }^\circ\text{C m}^{-1}$). A two-component
423 surface buoyancy flux is imposed, consisting of incoming short-wave radiation which is absorbed
424 using a Jerlov Type II absorption profile (Jerlov 1976), and an outgoing surface flux, held steady
425 in time. The idealized diurnal cycle is thus a repeating cycle of a function given by,

$$Q_{SWR}(t) = -Q_0 e^{-\left(\frac{\hat{t}-0.5}{0.25}\right)^2}, \quad (\text{A1})$$

426 where $Q_0 = 900 \text{ W m}^{-2}$, and \hat{t} ranges from 0 – 1 daily. A constant outgoing surface heat flux is
427 given by $Q_{LW} = 125 \text{ W m}^{-2}$. This particular profile leads to ~ 11 hours of heat flux into the ocean
428 (figure 15), which is an idealization taken to facilitate comparison between the model results and
429 theory. These surface fluxes are used for all runs, which ignores variations in solar heat flux as a
430 function of latitude and season that generally may result in variability at frequencies other than the
431 diurnal. Also important to note is that this forcing profile leads to a net heat flux into the ocean,
432 which in the 1D configuration utilized here can only lead to increasing temperature stratification
433 at the base of the turbulent boundary layer, affecting the evolution of the turbulent boundary layer

434 depth. This can be accounted for by imposition of a restoring interior heat flux (as in McWilliams
435 et al. 2009), however as we are here simply comparing the theory to the model based on diagnosed
436 fields, and are not concerned with the detailed evolution of the turbulent boundary layer depth, we
437 do not impose additional sources of interior cooling.

438 Surface wind stress is steady and in the zonal direction. The magnitude of the surface wind
439 stress is varied across runs, while the surface heat flux profile (figure 15) is not varied. This leads
440 to variations in the strength of the diurnal mixing cycle between runs. Turbulent viscosity is pa-
441 rameterized using KPP (Large et al. 1994), and calculated viscosities are output at every time step.
442 The calculation of surface layer viscosities in KPP couples vertical structure and time-dependence,
443 providing a more realistic model of near-surface turbulence than the simple dependence we require
444 in section 2. All model integrations are performed for 100 days with a 20 minute integration time
445 step.

446 The model output is principally useful as a point of qualitative comparison, as in figure 7. How-
447 ever, it is also possible to provide at least a basic assessment of the rectification effects discussed
448 in section 2c. To do this we run the above model repeatedly, varying latitude from $5^\circ - 90^\circ$ in
449 5° increments, and wind stress $\tau = 0.1 - 0.4 \text{ Nm}^{-2}$, holding the diurnal surface buoyancy flux
450 profiles constant across runs. In KPP the coupling of space-time variability in A_v means there is
451 no principled manner to effect the decomposition in order to estimate a steady-state solution for
452 calculation of rectification values. Here we make the simple ad hoc assumption that the vertical
453 structure can be taken as the time average $A_v(z)$ over the last-half of the integration period. We
454 then estimate δ by fitting a diurnally periodic sine function to the average A_v in the turbulent sur-
455 face boundary layer. Using these two estimates it is possible to compare the estimated rectification
456 to the theory.

457 Figure 16 shows the resulting estimate of the δ parameter for all model runs. There is a general
 458 increase in δ at low latitudes, emphasizing that this comparison is not an exhaustive exploration
 459 of the parameter space. Lower values of δ at any given latitude could be achieved by decreasing
 460 the diurnal variations in surface heat flux or increasing the surface wind stress. For KPP, the error
 461 in approximating $A_v(z, t)$ as $K(t)A(z)$ at a fixed depth z is a complex, non-monotonic, function of
 462 both δ and z/\bar{h} , the ratio of z to the time mean turbulent boundary layer depth. However, some
 463 insight into the limits of this decomposition comes from writing $A_v(z, t) = K(t)A(\sigma)$, where $\sigma =$
 464 $-z/h(t)$ is the rescaled vertical coordinate with a time varying turbulent boundary layer depth $h(t)$.
 465 Approximating this in a Taylor series gives $A_v(z, t) \approx K(t) \left(\overline{A(z)} + \partial A / \partial t|_{t=t_0} (t - t_0) \right)$, where the
 466 bar notation indicates the time mean value, which occurs at time t_0 . The assumption of space
 467 and time separability can then be posed as an assumption that $\partial A / \partial t|_{t=t_0} \ll \overline{A(z)}$, at all times, or
 468 equivalently, $\partial A / \partial \sigma|_{t=t_0} \partial \sigma / \partial t|_{t=t_0} \ll \overline{A(z)}$. Thus at a given depth, both the local vertical slope
 469 of the eddy viscosity, as well as the time rate of change of the boundary layer depth, will affect the
 470 errors in approximating the eddy viscosity in KPP as separable in time and space.

471 Despite these limitations, we find velocity rectification in the numerical model is reproduced
 472 remarkably well by the theory (figure 17), however shear rectification is greatly overestimated
 473 for values of $\delta > 0.8$. Several reasons for this are suggested. First, the method of estimating δ
 474 is somewhat arbitrary, and for instance, the coupling of spatial structure and time-dependence in
 475 KPP means that near-surface A_v is generally subject to smaller diurnal fluctuations than deeper in
 476 the boundary layer. Shear rectification is particularly sensitive at high δ (figure 12), and hence may
 477 be particularly sensitive to incorrect estimates of this parameter. Secondly, higher vertical modes
 478 contribute more strongly to shear rectification than velocity rectification. These higher modes, with
 479 their small vertical scale and associated strong shear, may be damped in a more realistic turbulence
 480 closure such as KPP, where wind-driven shear feeds back into the determination of A_v . Finally,

481 for the surface forcing used here, the cases of high δ tend to occur at low latitudes (figure 16),
 482 associated with the deeper boundary layers in KPP generated in response to periodic buoyancy
 483 forcing at low latitudes (McWilliams et al. 2009), which results in increasingly non-sinusoidal
 484 time-variability of A_V . Hence, some of the departure of the model results from the theory may
 485 implicate the time-varying structure of A_V as departing from the basic theoretical assumptions.

486 APPENDIX B

487 Errors for $f + n\omega \rightarrow 0$

488 As discussed in section 2, application of the WKBJ approximation requires that $Ek_n = \frac{A_0}{(f+n\omega)D^2}$
 489 remains small, so as to not violate eqs. (16) and (17). In this appendix we assess the error con-
 490 tributed to the total solution from the modes where $f \rightarrow \pm n\omega$, where mode $\mp n$ will have $Ek_n \rightarrow \infty$.
 491 For the diurnal frequency considered here this can occur only for modes $n = \pm 1, 2$, at latitudes 30°
 492 and 90° , respectively.

493 Each approximate solution for the vertical structure function, (24b), can be considered as $\Omega_n =$
 494 $\hat{\Omega}_n + E_n$, where the hat notation indicates the exact solution, and E_n represents errors associated
 495 with the WKBJ approximation. For the WKBJ approximation $E_n \sim Ek_n^{1/2}$. Utilizing this in the
 496 full summation, the error that the n^{th} mode contributes to the total solution, which we denote E_{T_n} ,
 497 will be proportional to,

$$E_{T_n} \sim \left(\frac{f}{f + n\omega} \right)^{1/2} J_n(\gamma_n) Ek_n^{1/2}. \quad (\text{B1})$$

498 Utilizing the definition of Ek_n , this can be rewritten as,

$$E_{T_n} \sim \frac{f}{f + n\omega} J_n(\gamma_n) Ek_0^{1/2}. \quad (\text{B2})$$

499 Taking the limit of equation (B2) as $f + n\omega \rightarrow 0$ gives, $|E_{T_n}| \sim |1/2Ek_0^{1/2}|$ if $n = \pm 1$ and $E_{T_n} \sim 0$
 500 if $n = \pm 2$. Thus, due to the behavior of the Bessel functions as their argument goes to zero,

501 the errors associated with these modes where the WKBJ approximation is formally invalid, are at
502 worst $O(Ek_0^{1/2})$, and ensuring the validity of the WKBJ approximation for $n = 0$ remains sufficient
503 to ensure validity for all modes.

504 **References**

505 Balmforth, N. J., and R. V. Craster, 2001: Geophysical Aspects of Non-Newtonian Fluid Mechan-
506 ics. *Geomorphological Fluid Mechanics*, N. J. Balmforth, and A. Provenzale, Eds., Vol. 582,
507 Springer Berlin Heidelberg, Berlin, Heidelberg, 34–51, URL [http://link.springer.com/10.1007/](http://link.springer.com/10.1007/3-540-45670-8_2)
508 [3-540-45670-8_2](http://link.springer.com/10.1007/3-540-45670-8_2).

509 Bender, C. M., and S. A. Orszag, 1978: *Advanced mathematical methods for scientists and engi-*
510 *neers*. Springer, New York.

511 Bernie, D. J., E. Guilyardi, G. Madec, J. M. Slingo, and S. J. Woolnough, 2007: Impact of resolv-
512 ing the diurnal cycle in an oceanatmosphere GCM. Part 1: a diurnally forced OGCM. *Climate*
513 *Dynamics*, **29** (6), 575–590, doi:10.1007/s00382-007-0249-6, URL [http://link.springer.com/10.](http://link.springer.com/10.1007/s00382-007-0249-6)
514 [1007/s00382-007-0249-6](http://link.springer.com/10.1007/s00382-007-0249-6).

515 Bernie, D. J., E. Guilyardi, G. Madec, J. M. Slingo, S. J. Woolnough, and J. Cole, 2008: Im-
516 pact of resolving the diurnal cycle in an oceanatmosphere GCM. Part 2: A diurnally cou-
517 pled CGCM. *Climate Dynamics*, **31** (7-8), 909–925, doi:10.1007/s00382-008-0429-z, URL
518 <http://link.springer.com/10.1007/s00382-008-0429-z>.

519 Blackadar, A. K., 1957: Boundary layer wind maxima and their significance for the growth of
520 nocturnal inversions. *Bull. Amer. Meteor. Soc.*, **38** (5), 283–290.

- 521 Brainerd, K. E., and M. C. Gregg, 1993: Diurnal restratification and turbulence in the oceanic
522 surface mixed layer: 1. Observations. *Journal of Geophysical Research*, **98 (C12)**, 22 645, doi:
523 10.1029/93JC02297, URL <http://doi.wiley.com/10.1029/93JC02297>.
- 524 Buajitti, K., and A. K. Blackadar, 1957: Theoretical studies of diurnal wind-structure variations in
525 the planetary boundary layer. *Quarterly Journal of the Royal Meteorological Society*, **83 (358)**,
526 486–500, doi:10.1002/qj.49708335804, URL <http://doi.wiley.com/10.1002/qj.49708335804>.
- 527 Cannon, J. R., 1984: *The one-dimensional heat equation*, Encyclopedia of mathematics and its
528 applications, Vol. 23. Cambridge University Press, Cambridge, U.K.
- 529 Chen, S. S., and R. A. Houze, 1997: Diurnal variation and life-cycle of deep convective sys-
530 tems over the tropical Pacific warm pool. *Quarterly Journal of the Royal Meteorological So-*
531 *ciety*, **123 (538)**, 357–388, doi:10.1002/qj.49712353806, URL [http://doi.wiley.com/10.1002/qj.](http://doi.wiley.com/10.1002/qj.49712353806)
532 [49712353806](http://doi.wiley.com/10.1002/qj.49712353806).
- 533 Clayson, C. A., and A. Chen, 2002: Sensitivity of a Coupled Single-Column Model in the Tropics
534 to Treatment of the Interfacial Parameterizations. *Journal of Climate*, **15 (14)**, 1805–1831, doi:
535 10.1175/1520-0442(2002)015<1805:SOACSC>2.0.CO;2, URL [http://journals.ametsoc.org/doi/](http://journals.ametsoc.org/doi/abs/10.1175/1520-0442%282002%29015%3C1805%3ASOACSC%3E2.0.CO%3B2)
536 [abs/10.1175/1520-0442%282002%29015%3C1805%3ASOACSC%3E2.0.CO%3B2](http://journals.ametsoc.org/doi/abs/10.1175/1520-0442%282002%29015%3C1805%3ASOACSC%3E2.0.CO%3B2).
- 537 Csanady, G. T., and P. T. Shaw, 1980: The evolution of a turbulent Ekman layer. *Journal of*
538 *Geophysical Research*, **85 (C3)**, 1537, doi:10.1029/JC085iC03p01537, URL [http://doi.wiley.](http://doi.wiley.com/10.1029/JC085iC03p01537)
539 [com/10.1029/JC085iC03p01537](http://doi.wiley.com/10.1029/JC085iC03p01537).
- 540 Dai, A., and K. E. Trenberth, 2004: The Diurnal Cycle and Its Depiction in the Community
541 Climate System Model. *Journal of Climate*, **17 (5)**, 930–951, doi:10.1175/1520-0442(2004)

542 017(0930:TDCAID)2.0.CO;2, URL [http://journals.ametsoc.org/doi/abs/10.1175/1520-0442%](http://journals.ametsoc.org/doi/abs/10.1175/1520-0442%282004%29017%3C0930%3ATDCAID%3E2.0.CO%3B2)
543 [282004%29017%3C0930%3ATDCAID%3E2.0.CO%3B2](http://journals.ametsoc.org/doi/abs/10.1175/1520-0442%282004%29017%3C0930%3ATDCAID%3E2.0.CO%3B2).

544 Danabasoglu, G., W. G. Large, J. J. Tribbia, P. R. Gent, B. P. Briegleb, and J. C. McWilliams, 2006:
545 Diurnal Coupling in the Tropical Oceans of CCSM3. *Journal of Climate*, **19** (11), 2347–2365,
546 doi:10.1175/JCLI3739.1, URL <http://journals.ametsoc.org/doi/abs/10.1175/JCLI3739.1>.

547 Davis, R., R. de Szoeko, and P. Niiler, 1981: Variability in the upper ocean during MILE. Part II:
548 Modeling the mixed layer response. *Deep Sea Research Part A. Oceanographic Research Pa-*
549 *pers*, **28** (12), 1453–1475, doi:10.1016/0198-0149(81)90092-3, URL [http://linkinghub.elsevier.](http://linkinghub.elsevier.com/retrieve/pii/0198014981900923)
550 [com/retrieve/pii/0198014981900923](http://linkinghub.elsevier.com/retrieve/pii/0198014981900923).

551 Elipot, S., and S. T. Gille, 2009: Ekman layers in the Southern Ocean: spectral models and ob-
552 servations, vertical viscosity and boundary layer depth. *Ocean Science*, **5** (2), 115–139, doi:
553 10.5194/os-5-115-2009, URL <http://www.ocean-sci.net/5/115/2009/>.

554 Grisogono, B., 1995: A generalized Ekman layer profile with gradually varying eddy diffusivities.
555 *Quarterly Journal of the Royal Meteorological Society*, **121** (522), 445–453, doi:10.1002/qj.
556 49712152211, URL <http://doi.wiley.com/10.1002/qj.49712152211>.

557 Huang, N. E., 1979: On surface drift currents in the ocean. *Journal of Fluid Mechanics*, **91** (01),
558 191, doi:10.1017/S0022112079000112.

559 Jerlov, N. G., 1976: *Marine Optics*. Elsevier, Amsterdam.

560 Kawai, Y., and A. Wada, 2007: Diurnal sea surface temperature variation and its impact on the
561 atmosphere and ocean: A review. *Journal of Oceanography*, **63** (5), 721–744, doi:10.1007/
562 s10872-007-0063-0, URL <http://link.springer.com/10.1007/s10872-007-0063-0>.

- 563 Kim, S. Y., P. M. Kosro, and A. L. Kurapov, 2014: Evaluation of directly wind-coherent near-
564 inertial surface currents off Oregon using a statistical parameterization and analytical and
565 numerical models. *Journal of Geophysical Research: Oceans*, **119** (10), 6631–6654, doi:
566 10.1002/2014JC010115, URL <http://doi.wiley.com/10.1002/2014JC010115>.
- 567 Large, W. G., J. C. McWilliams, and S. C. Doney, 1994: Oceanic vertical mixing: A review and
568 a model with a nonlocal boundary layer parameterization. *Reviews of Geophysics*, **32** (4), 363,
569 doi:10.1029/94RG01872, URL <http://doi.wiley.com/10.1029/94RG01872>.
- 570 Lenn, Y.-D., and T. K. Chereskin, 2009: Observations of Ekman Currents in the Southern Ocean.
571 *Journal of Physical Oceanography*, **39** (3), 768–779, doi:10.1175/2008JPO3943.1, URL [http://](http://journals.ametsoc.org/doi/abs/10.1175/2008JPO3943.1)
572 journals.ametsoc.org/doi/abs/10.1175/2008JPO3943.1.
- 573 Lewis, D., and S. Belcher, 2004: Time-dependent, coupled, Ekman boundary layer solutions in-
574 corporating Stokes drift. *Dynamics of Atmospheres and Oceans*, **37** (4), 313–351, doi:10.1016/j.
575 dynatmoce.2003.11.001, URL <http://linkinghub.elsevier.com/retrieve/pii/S0377026503000605>.
- 576 Mangat, P. S., and B. T. Molloy, 1994: Prediction of long term chloride concentration in
577 concrete. *Materials and Structures*, **27** (6), 338–346, doi:10.1007/BF02473426, URL [http://](http://www.springerlink.com/index/10.1007/BF02473426)
578 www.springerlink.com/index/10.1007/BF02473426.
- 579 Marshall, J., C. Hill, L. Perelman, and A. Adcroft, 1997: Hydrostatic, quasi-hydrostatic, and
580 nonhydrostatic ocean modeling. *Journal of Geophysical Research*, **102** (C3), 5733, doi:10.1029/
581 96JC02776, URL <http://doi.wiley.com/10.1029/96JC02776>.
- 582 McCreary, J. P., K. E. Kohler, R. R. Hood, S. Smith, J. Kindle, A. S. Fischer, and R. A. Weller,
583 2001: Influences of diurnal and intraseasonal forcing on mixed-layer and biological variability

584 in the central Arabian Sea. *Journal of Geophysical Research*, **106 (C4)**, 7139, doi:10.1029/
585 2000JC900156, URL <http://doi.wiley.com/10.1029/2000JC900156>.

586 McWilliams, J. C., and E. Huckle, 2006: Ekman Layer Rectification. *Journal of Physical*
587 *Oceanography*, **36 (8)**, 1646–1659, doi:10.1175/JPO2912.1, URL [http://journals.ametsoc.org/
588 doi/abs/10.1175/JPO2912.1](http://journals.ametsoc.org/doi/abs/10.1175/JPO2912.1).

589 McWilliams, J. C., E. Huckle, and A. F. Shchepetkin, 2009: Buoyancy Effects in a Strat-
590 ified Ekman Layer. *Journal of Physical Oceanography*, **39 (10)**, 2581–2599, doi:10.1175/
591 2009JPO4130.1, URL <http://journals.ametsoc.org/doi/abs/10.1175/2009JPO4130.1>.

592 O’Brien, J. J., 1970: A Note on the Vertical Structure of the Eddy Exchange Coefficient in
593 the Planetary Boundary Layer. *Journal of the Atmospheric Sciences*, **27 (8)**, 1213–1215, doi:
594 10.1175/1520-0469(1970)027<1213:ANOTVS>2.0.CO;2, URL [http://journals.ametsoc.org/doi/
595 abs/10.1175/1520-0469%281970%29027%3C1213%3AANOTVS%3E2.0.CO%3B2](http://journals.ametsoc.org/doi/abs/10.1175/1520-0469%281970%29027%3C1213%3AANOTVS%3E2.0.CO%3B2).

596 Price, J. F., and M. A. Sundermeyer, 1999: Stratified Ekman layers. *Journal of Geophysical*
597 *Research*, **104 (C9)**, 20 467, doi:10.1029/1999JC900164, URL [http://doi.wiley.com/10.1029/
598 1999JC900164](http://doi.wiley.com/10.1029/1999JC900164).

599 Price, J. F., R. A. Weller, and R. Pinkel, 1986: Diurnal cycling: Observations and models of the
600 upper ocean response to diurnal heating, cooling, and wind mixing. *Journal of Geophysical*
601 *Research*, **91 (C7)**, 8411, doi:10.1029/JC091iC07p08411, URL [http://doi.wiley.com/10.1029/
602 JC091iC07p08411](http://doi.wiley.com/10.1029/JC091iC07p08411).

603 Raschle, N., and F. Ardhuin, 2009: Drift and mixing under the ocean surface revisited: Stratified
604 conditions and model-data comparisons. *Journal of Geophysical Research*, **114 (C2)**, doi:10.
605 1029/2007JC004466, URL <http://doi.wiley.com/10.1029/2007JC004466>.

- 606 Sheih, C. M., 1972: A Theoretical Study of the Diurnal Wind Variations in the Planetary Boundary
607 Layer. *Journal of the Atmospheric Sciences*, **29** (5), 995–998, doi:10.1175/1520-0469(1972)
608 029(0995:ATSOTD)2.0.CO;2, URL [http://journals.ametsoc.org/doi/abs/10.1175/1520-0469%](http://journals.ametsoc.org/doi/abs/10.1175/1520-0469%281972%29029%3C0995%3AATSOTD%3E2.0.CO%3B2)
609 [281972%29029%3C0995%3AATSOTD%3E2.0.CO%3B2](http://journals.ametsoc.org/doi/abs/10.1175/1520-0469%281972%29029%3C0995%3AATSOTD%3E2.0.CO%3B2).
- 610 Shinoda, T., 2005: Impact of the Diurnal Cycle of Solar Radiation on Intraseasonal SST
611 Variability in the Western Equatorial Pacific. *Journal of Climate*, **18** (14), 2628–2636, doi:
612 10.1175/JCLI3432.1, URL <http://journals.ametsoc.org/doi/abs/10.1175/JCLI3432.1>.
- 613 Singh, M. P., R. T. McNider, and J. T. Lin, 1993: An analytical study of diurnal wind-
614 structure variations in the boundary layer and the low-level nocturnal jet. *Boundary-Layer Me-*
615 *teorology*, **63** (4), 397–423, doi:10.1007/BF00705360, URL [http://link.springer.com/10.1007/](http://link.springer.com/10.1007/BF00705360)
616 [BF00705360](http://link.springer.com/10.1007/BF00705360).
- 617 Skeel, R. D., and M. Berzins, 1990: A Method for the Spatial Discretization of Parabolic Equations
618 in One Space Variable. *SIAM Journal on Scientific and Statistical Computing*, **11** (1), 1–32, doi:
619 10.1137/0911001, URL <http://epubs.siam.org/doi/abs/10.1137/0911001>.
- 620 Smyth, W., 1854: *The Mediterranean: A Memoir, Physical, Historical and Nautical*. J.W. Parker
621 and Son, London, U.K.
- 622 Smyth, W. D., J. N. Moum, L. Li, and S. A. Thorpe, 2013: Diurnal Shear Instability, the
623 Descent of the Surface Shear Layer, and the Deep Cycle of Equatorial Turbulence. *Jour-*
624 *nal of Physical Oceanography*, **43** (11), 2432–2455, doi:10.1175/JPO-D-13-089.1, URL [http:](http://journals.ametsoc.org/doi/abs/10.1175/JPO-D-13-089.1)
625 [//journals.ametsoc.org/doi/abs/10.1175/JPO-D-13-089.1](http://journals.ametsoc.org/doi/abs/10.1175/JPO-D-13-089.1).
- 626 Stommel, H., K. Saunders, W. Simmons, and J. Cooper, 1969: Observations of the diurnal ther-
627 mocline. *Deep Sea Res*, **16**, 269–284.

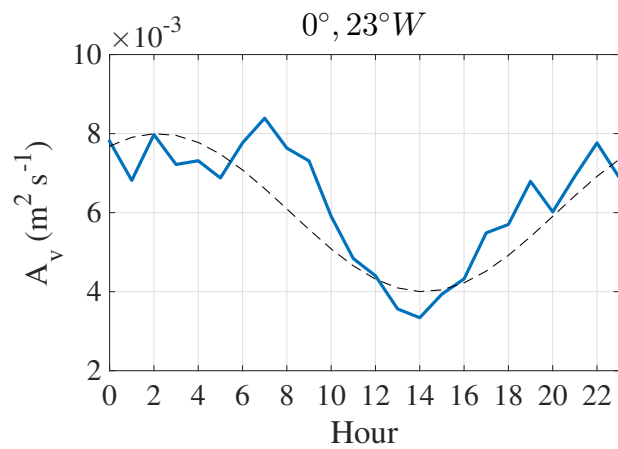
- 628 Tan, Z.-M., and M. M. Farahani, 1998: An analytical study of the diurnal variations of wind in
629 a semi-geostrophic Ekman boundary layer model. *Boundary-Layer Meteorology*, **86** (2), 313–
630 332, URL <http://link.springer.com/article/10.1023/A:1000694732459>.
- 631 Temme, N. M., 1996: *Special functions: an introduction to the classical functions of mathematical*
632 *physics*. Wiley, New York.
- 633 Vallis, G. K., 2006: *Atmospheric and oceanic fluid dynamics: fundamentals and large-scale cir-*
634 *culation*. Cambridge University Press, Cambridge, oCLC: ocm70671784.
- 635 Van de Wiel, B. J. H., A. F. Moene, G. J. Steeneveld, P. Baas, F. C. Bosveld, and A. A. M.
636 Holtslag, 2010: A Conceptual View on Inertial Oscillations and Nocturnal Low-Level Jets.
637 *Journal of the Atmospheric Sciences*, **67** (8), 2679–2689, doi:10.1175/2010JAS3289.1, URL
638 <http://journals.ametsoc.org/doi/abs/10.1175/2010JAS3289.1>.
- 639 Weller, R. A., and A. J. Plueddemann, 1996: Observations of the vertical structure of the oceanic
640 boundary layer. *Journal of Geophysical Research*, **101** (C4), 8789, doi:10.1029/96JC00206,
641 URL <http://doi.wiley.com/10.1029/96JC00206>.
- 642 Wenegrat, J. O., 2015: Ocean Boundary Layer Dynamics and Air-Sea Interaction. Ph.D. Thesis,
643 University of Washington, Seattle, WA, URL <http://hdl.handle.net/1773/35286>.
- 644 Wenegrat, J. O., and M. J. McPhaden, 2015: Dynamics of the surface layer diurnal cycle in the
645 equatorial Atlantic Ocean (0, 23W). *Journal of Geophysical Research: Oceans*, **120** (1), 563–
646 581, doi:10.1002/2014JC010504, URL <http://doi.wiley.com/10.1002/2014JC010504>.
- 647 Wenegrat, J. O., and M. J. McPhaden, 2016: Wind, Waves, and Fronts: Frictional Effects in a
648 Generalized Ekman Model. *Journal of Physical Oceanography*, **46** (2), 371–394, doi:10.1175/
649 JPO-D-15-0162.1, URL <http://journals.ametsoc.org/doi/abs/10.1175/JPO-D-15-0162.1>.

- 650 Wenegrat, J. O., M. J. McPhaden, and R.-C. Lien, 2014: Wind stress and near-surface shear in
651 the equatorial Atlantic Ocean. *Geophysical Research Letters*, **41** (4), 1226–1231, doi:10.1002/
652 2013GL059149, URL <http://doi.wiley.com/10.1002/2013GL059149>.
- 653 Zhang, Y., and Z.-M. Tan, 2002: The diurnal wind variation in a variable eddy viscosity semi-
654 geostrophic Ekman boundary-layer model: Analytical study. *Meteorology and Atmospheric*
655 *Physics*, **81** (3-4), 207–217, URL <http://link.springer.com/article/10.1007/s00703-001-0542-6>.
- 656 Zikanov, O., D. N. Slinn, and M. R. Dhanak, 2003: Large-eddy simulations of the wind-
657 induced turbulent Ekman layer. *Journal of Fluid Mechanics*, **495**, 343–368, doi:10.1017/
658 S0022112003006244, URL http://www.journals.cambridge.org/abstract_S0022112003006244.

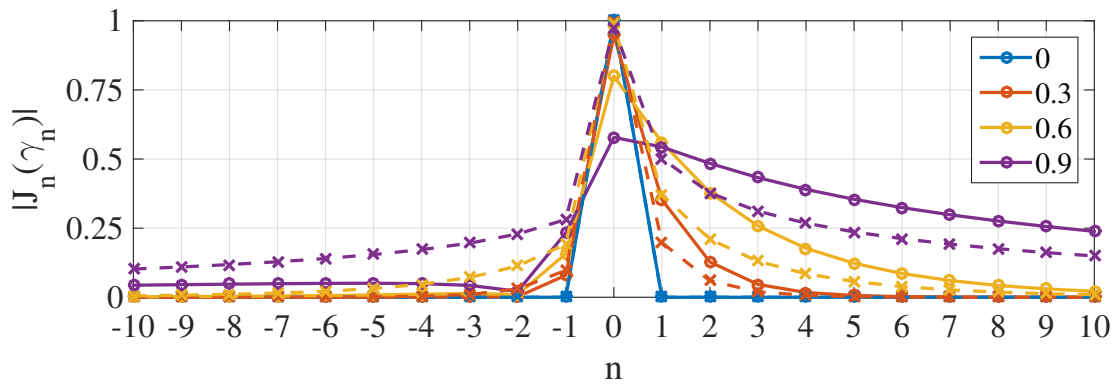
LIST OF FIGURES

659		
660	Fig. 1.	Composite diurnal cycle in A_v at 0° , $23^\circ W$, $z = -5.6$ m, inferred from observations (blue) from 13 October 2008 through 6 January 2009, as discussed in Wenegrat and McPhaden (2015, their section 4.1). Also shown is a sinusoidal approximation to the composite diurnal cycle (dashed, with $A_{v0} = 6 \times 10^{-3} \text{ m}^2 \text{ s}^{-1}$ and $\delta = 0.3$). 36
661		
662		
663		
664	Fig. 2.	Bessel function wind-stress coupling coefficients for the first ± 10 modes at 10° (dashed) and 50° (solid), for values of δ as indicated. 37
665		
666	Fig. 3.	Time dependence for the first ± 20 modes, assuming $\delta = 0.75$, and latitude 45° . Top, real components, bottom: imaginary components. 38
667		
668	Fig. 4.	Example diurnal cycle velocity hodograph for vertically uniform A_v , with $h_{Ek} = 14$ m and $\delta = 0.75$. At each depth the velocity vector traces a closed contour over one 24 hour period, plotted for selected depths, beginning at $z = 0$ and decreasing in increments of 2 m (thin lines, with color scale indicating hour of day). The time averaged diurnal velocity is shown (heavy black), as is the steady state solution (dashed black). All velocities are normalized by the steady-state Ekman surface velocity. 39
669		
670		
671		
672		
673		
674	Fig. 5.	Modeled diurnal cycle at $45^\circ N$, for vertically uniform A_v , and $\delta = 0.75$. Velocities are normalized by $\tau/(\rho\sqrt{fA_{v0}})$, and shear normalized by $2\tau/(\rho A_{v0})$, twice the surface shear for the constant viscosity solution. Contours are non-linearly spaced to emphasize the deep variability. 40
675		
676		
677		
678	Fig. 6.	Zonal momentum balance terms for the same case considered in figure 5, with values normalized by $\tau/(\rho h_{Ek0})$ 41
679		
680	Fig. 7.	Comparison of numerical model and theoretical solution for $45^\circ N$, with $\tau = 0.1 \text{ N m}^{-2}$. Parameters for the theoretical solution are diagnosed from the numerical solution following the discussion in Appendix A, and the boundary value problems, equation (11), are solved numerically rather than utilizing the WKBJ approximate solution. Times of negative (red) and positive (blue) net surface buoyancy flux are indicated in each plot for $z > 0$ 42
681		
682		
683		
684		
685	Fig. 8.	Effect of varying δ with parameters and normalization as given for figure 5. 43
686	Fig. 9.	Effect of varying latitude, with parameters and normalization as given for figure 5. Note both the velocity and depth normalizations are a function of latitude. 44
687		
688	Fig. 10.	Vertical structure in A_v modifies the diurnal cycle solutions. Right panels are for a modified Gaussian A_v profile ($A_v(z) = A_{v0}e^{-0.5(z/0.25h_{Ek})} + \epsilon$, orange line in left plot), center panels are for a vertically uniform A_v , taken as the mean value of the modified Gaussian profile between $z = 0$ and $z = -h_{Ek}$ (blue line in left plot). The vertical coordinate is normalized using $h_{Ek} = 0.7\sqrt{\tau/\rho}/f$, velocity is normalized by $\tau/(\rho\sqrt{fA_{v0}})$, shear is normalized by $4\tau/(\rho A_{v0})$, and $\delta = 0.75$. Solutions to (11) were found numerically. 45
689		
690		
691		
692		
693		
694	Fig. 11.	Angle of the time-averaged surface currents relative to the surface wind stress. Negative values indicate anticyclonic rotation. 46
695		
696	Fig. 12.	Contour plot of the parameter dependence for the theoretical normalized rectification values, equation (30), for velocity (left) and shear (right). 47
697		

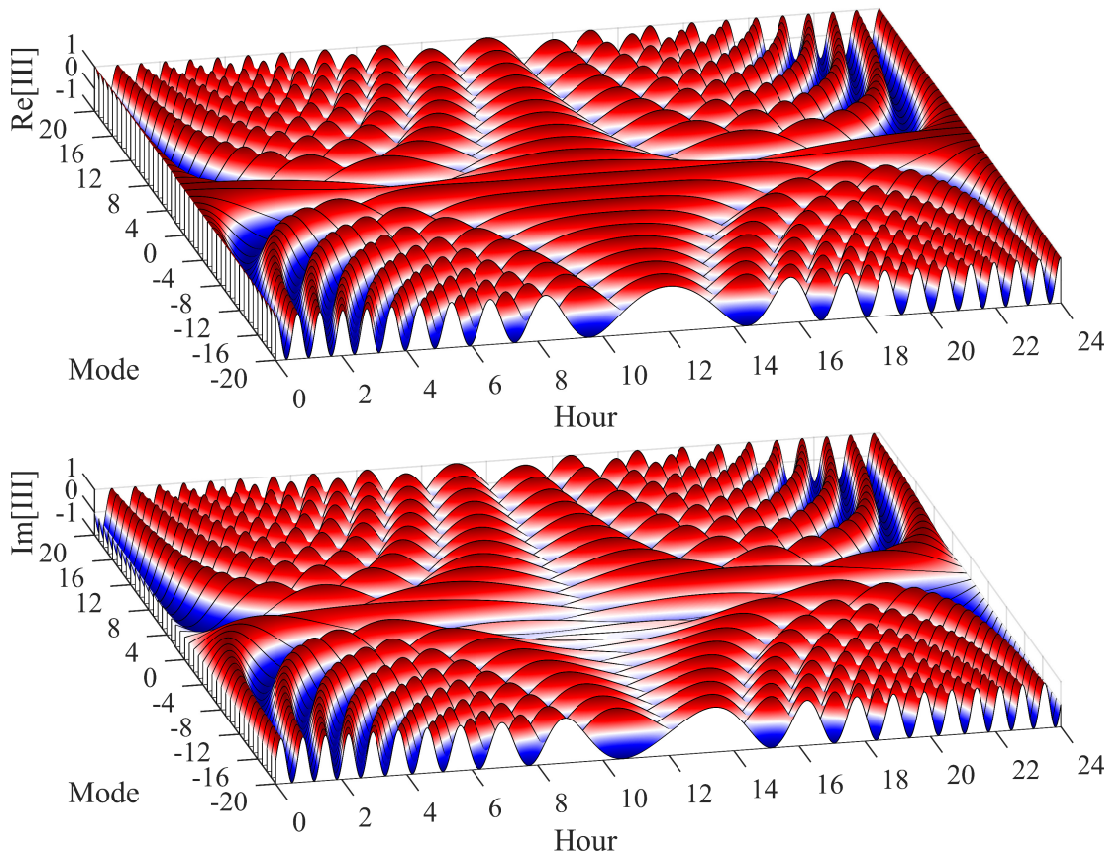
698	Fig. 13.	Validation of the rectification implied by the time-periodic solution against a numerical solution of the initial-boundary-value problem as discussed in section 3c.	48
699			
700	Fig. 14.	Effective eddy viscosities inferred from the time mean solution for vertically uniform A_v , as defined by equation (33), with various δ values as shown in the legend. $A_{v_{Eff}}$ magnitudes are normalized by the true A_v , and angles ($^\circ$) are relative to the local mean-shear direction. . . .	49
701			
702			
703	Fig. 15.	Idealized diurnal cycle of net surface heat flux used to force the numerical model discussed in Appendix A.	50
704			
705	Fig. 16.	Diagnosed magnitude of the diurnal A_v cycle from the numerical model, calculated as described in Appendix A, as a function of latitude and surface wind-stress (legend).	51
706			
707	Fig. 17.	Comparison of inferred rectification in the numerical model against theoretical predictions for velocity (left) and shear (right). In each plot, colorscale gives the inferred δ , symbol shape gives the magnitude of the surface wind-stress as shown in the legend, and the dashed line indicates the 1-1 line. Correlation coefficients are shown above each plot.	52
708			
709			
710			



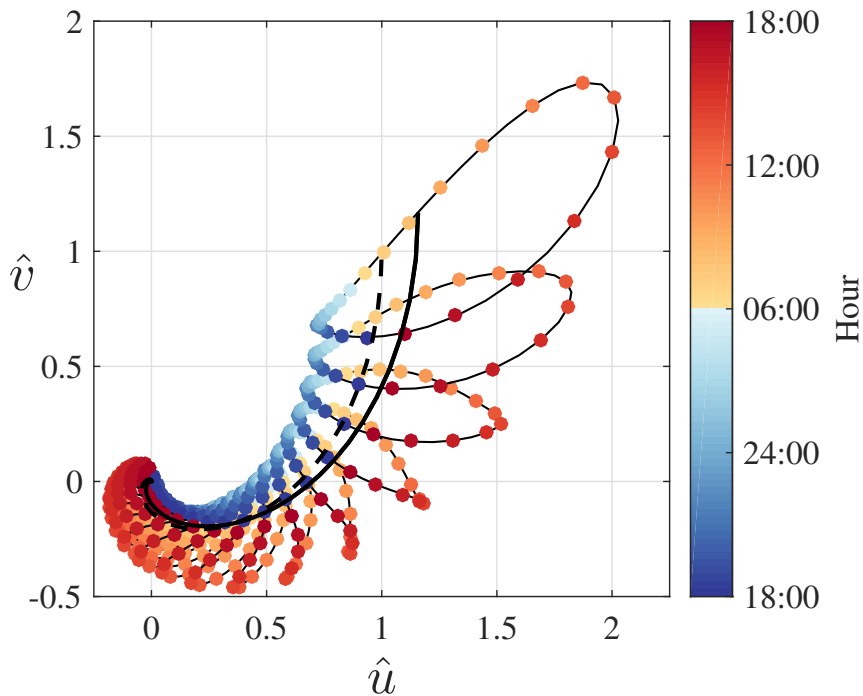
711 FIG. 1. Composite diurnal cycle in A_v at 0° , $23^\circ W$, $z = -5.6 \text{ m}$, inferred from observations (blue) from 13
 712 October 2008 through 6 January 2009, as discussed in Wenegrat and McPhaden (2015, their section 4.1). Also
 713 shown is a sinusoidal approximation to the composite diurnal cycle (dashed, with $A_{v_0} = 6 \times 10^{-3} \text{ m}^2 \text{ s}^{-1}$ and
 714 $\delta = 0.3$).



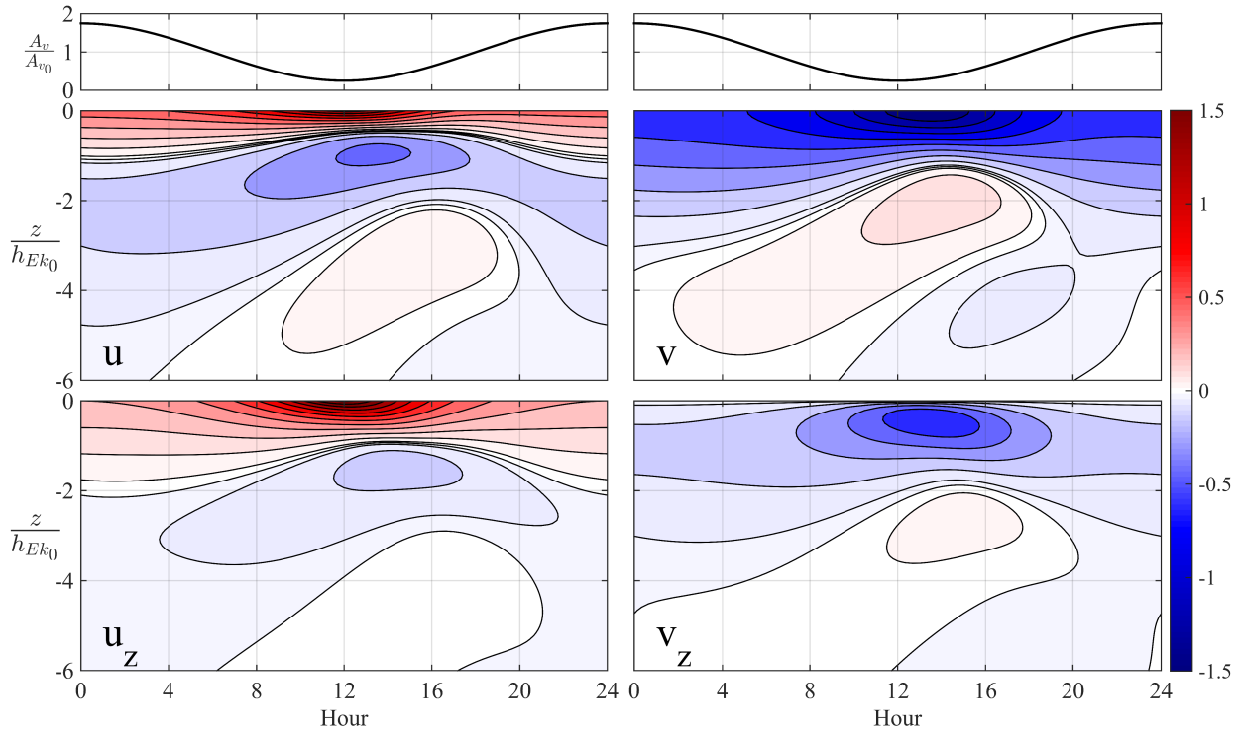
715 FIG. 2. Bessel function wind-stress coupling coefficients for the first ± 10 modes at 10° (dashed) and 50°
 716 (solid), for values of δ as indicated.



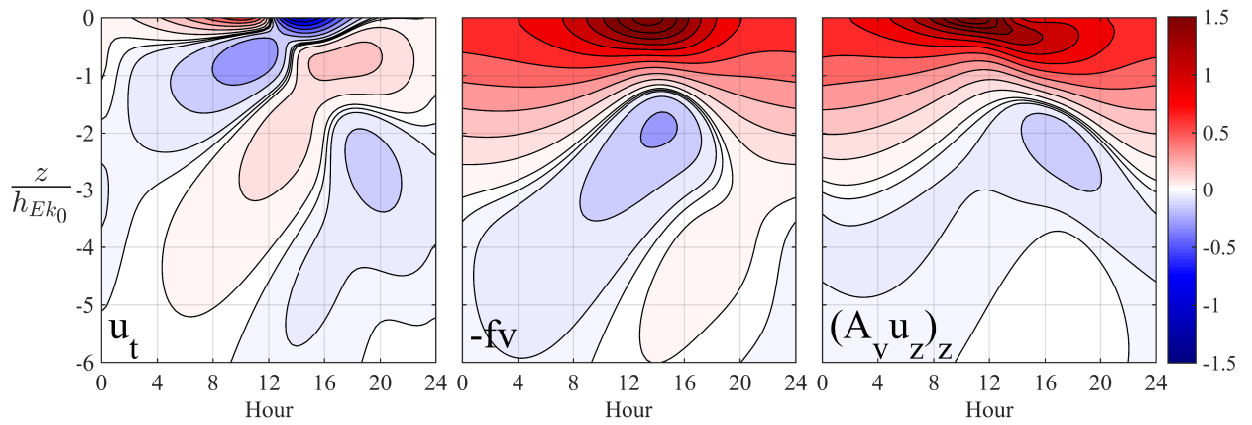
717 FIG. 3. Time dependence for the first ± 20 modes, assuming $\delta = 0.75$, and latitude 45° . Top, real components,
 718 bottom: imaginary components.



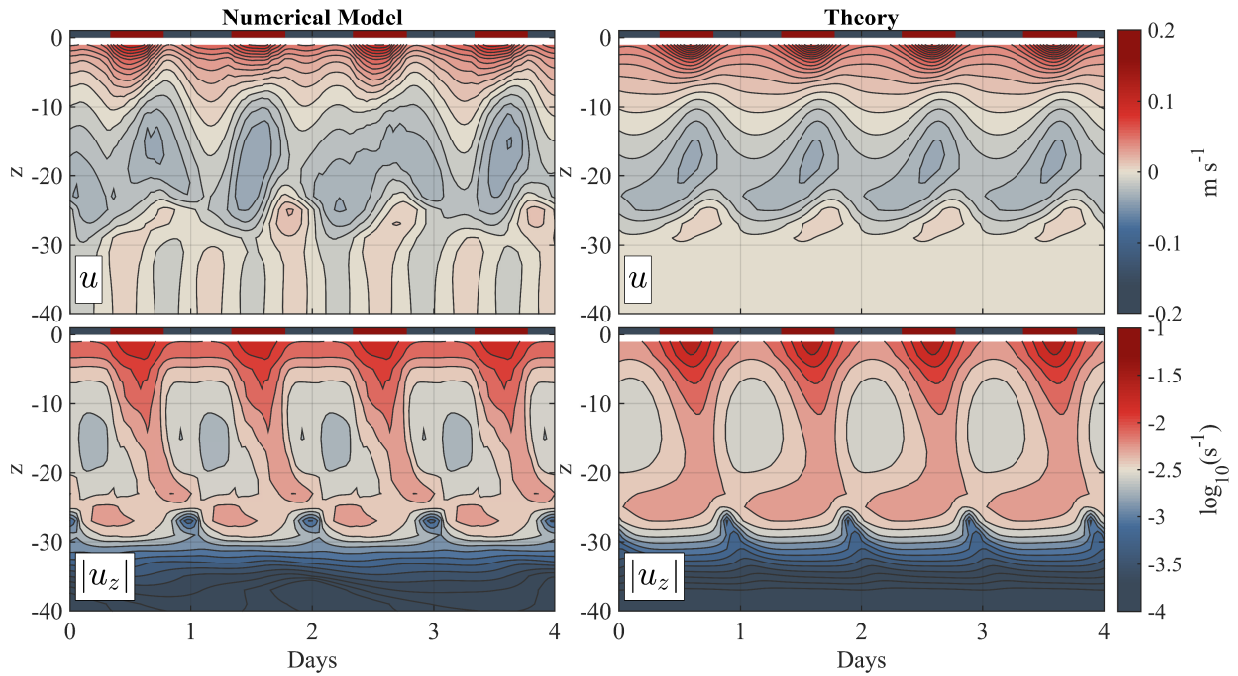
719 FIG. 4. Example diurnal cycle velocity hodograph for vertically uniform A_V , with $h_{Ek} = 14$ m and $\delta = 0.75$.
 720 At each depth the velocity vector traces a closed contour over one 24 hour period, plotted for selected depths,
 721 beginning at $z = 0$ and decreasing in increments of 2 m (thin lines, with color scale indicating hour of day).
 722 The time averaged diurnal velocity is shown (heavy black), as is the steady state solution (dashed black). All
 723 velocities are normalized by the steady-state Ekman surface velocity.



724 FIG. 5. Modeled diurnal cycle at $45^\circ N$, for vertically uniform A_v , and $\delta = 0.75$. Velocities are normalized by
 725 $\tau/(\rho\sqrt{fA_{v0}})$, and shear normalized by $2\tau/(\rho A_{v0})$, twice the surface shear for the constant viscosity solution.
 726 Contours are non-linearly spaced to emphasize the deep variability.



727 FIG. 6. Zonal momentum balance terms for the same case considered in figure 5, with values normalized by
 728 $\tau/(\rho h_{Ek_0})$.



729 FIG. 7. Comparison of numerical model and theoretical solution for $45^\circ N$, with $\tau = 0.1 \text{ N m}^{-2}$. Parameters for
 730 the theoretical solution are diagnosed from the numerical solution following the discussion in Appendix A, and
 731 the boundary value problems, equation (11), are solved numerically rather than utilizing the WKBJ approximate
 732 solution. Times of negative (red) and positive (blue) net surface buoyancy flux are indicated in each plot for
 733 $z > 0$.

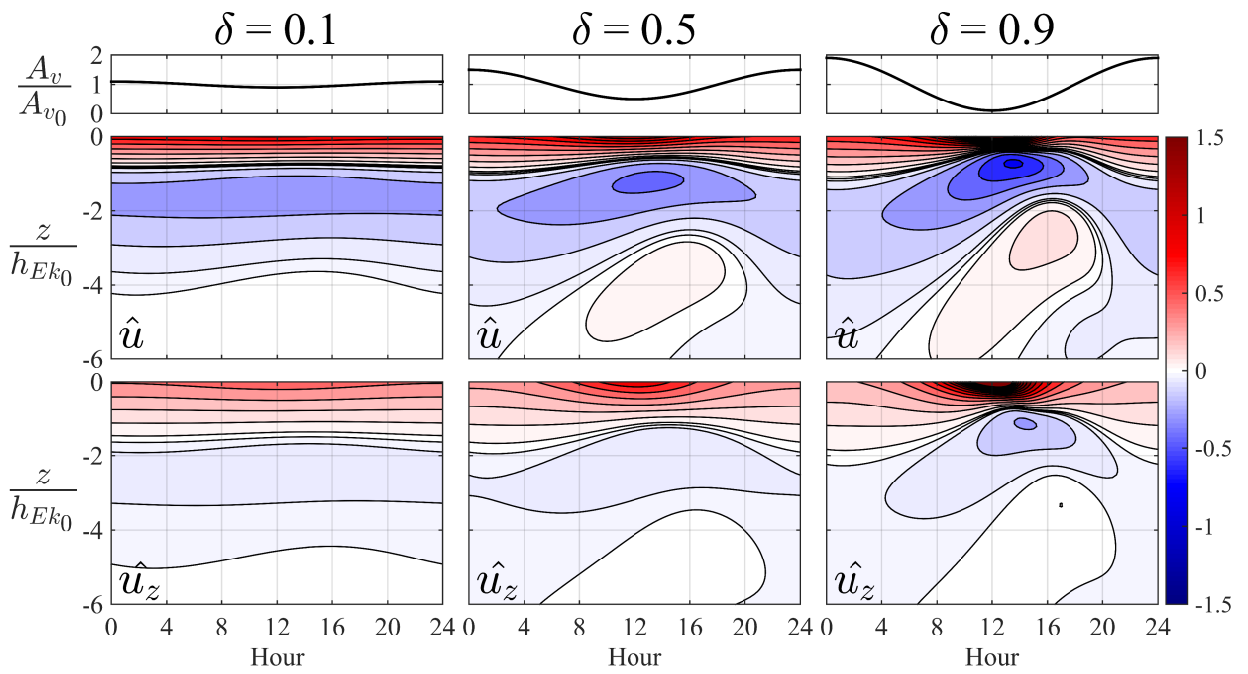
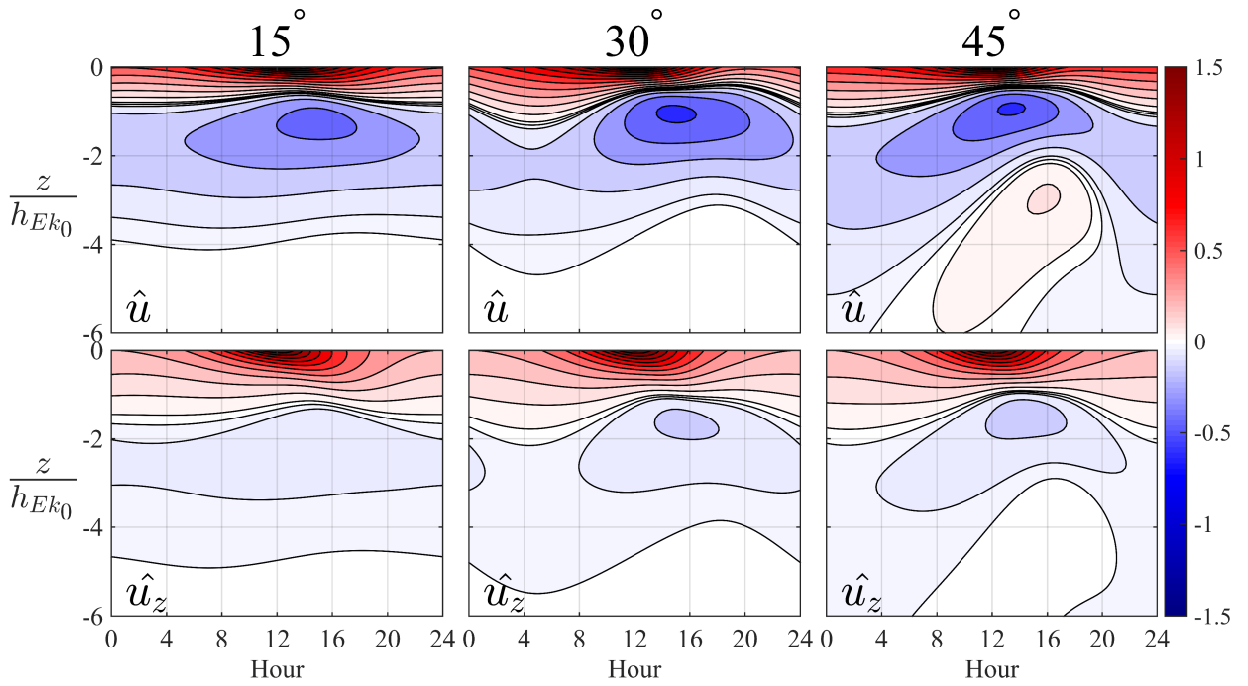
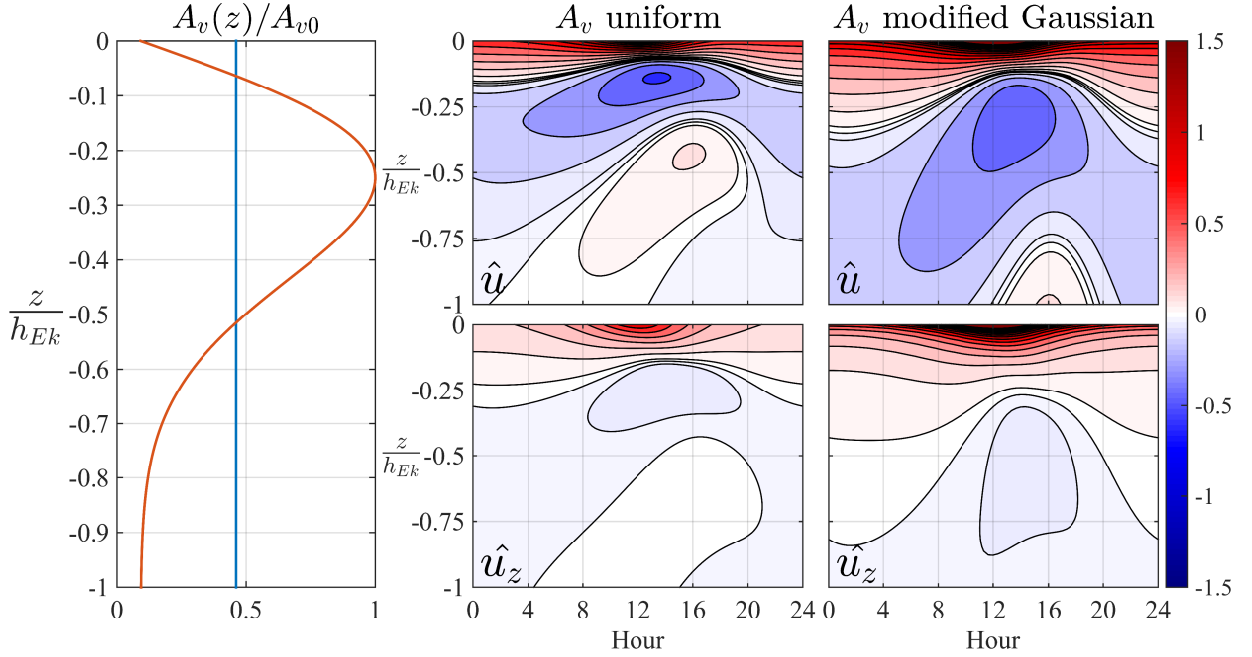


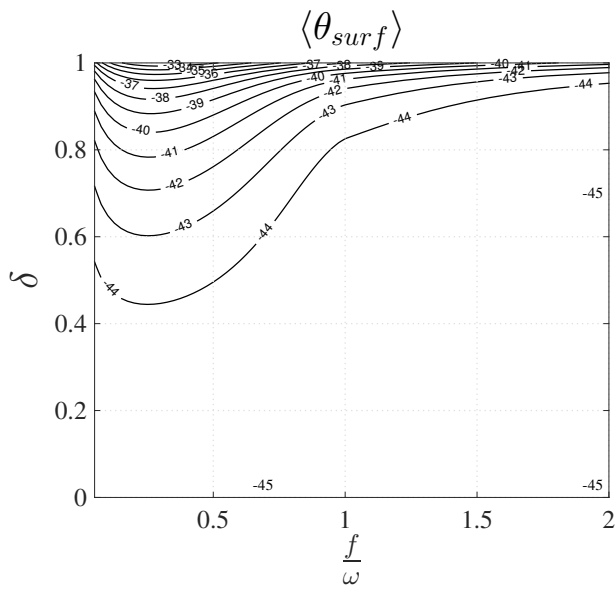
FIG. 8. Effect of varying δ with parameters and normalization as given for figure 5.



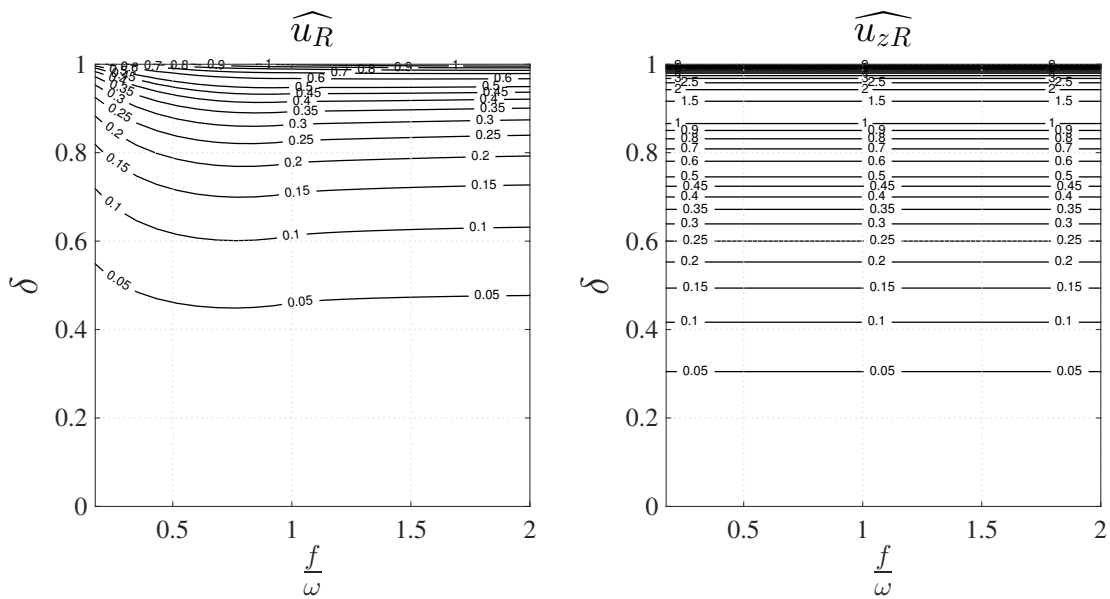
734 FIG. 9. Effect of varying latitude, with parameters and normalization as given for figure 5. Note both the
 735 velocity and depth normalizations are a function of latitude.



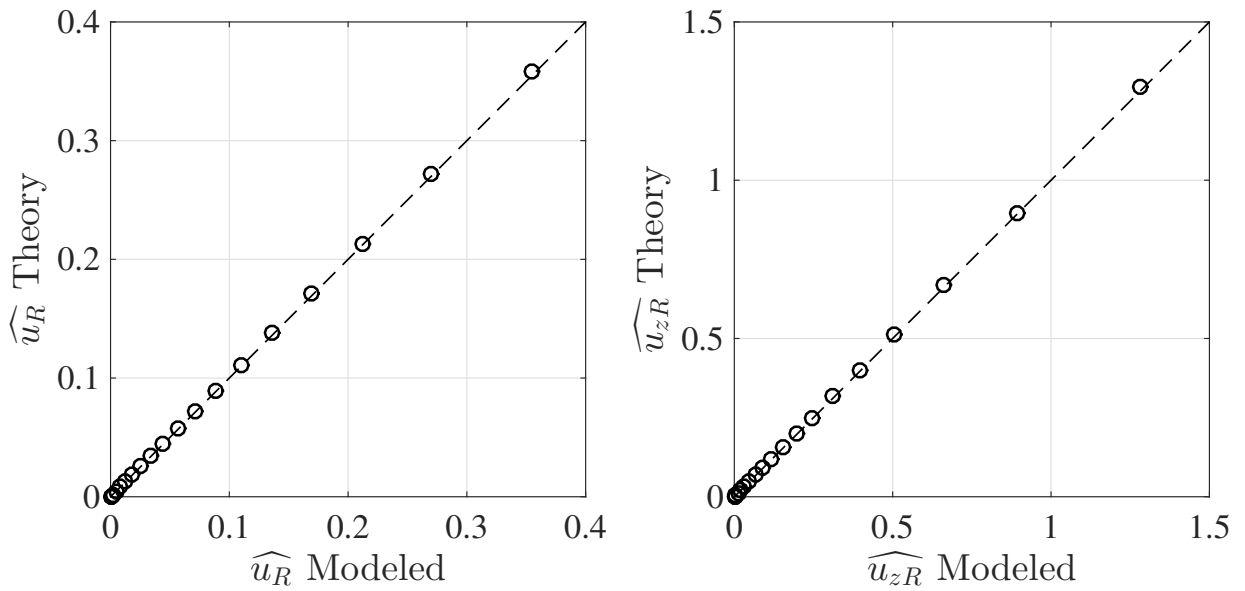
736 FIG. 10. Vertical structure in A_v modifies the diurnal cycle solutions. Right panels are for a modified Gaussian
737 A_v profile ($A_v(z) = A_{v0}e^{-0.5(z/0.25h_{Ek})} + \varepsilon$, orange line in left plot), center panels are for a vertically uniform A_v ,
738 taken as the mean value of the modified Gaussian profile between $z = 0$ and $z = -h_{Ek}$ (blue line in left plot).
739 The vertical coordinate is normalized using $h_{Ek} = 0.7\sqrt{\tau/\rho}/f$, velocity is normalized by $\tau/(\rho\sqrt{fA_{v0}})$, shear
740 is normalized by $4\tau/(\rho A_{v0})$, and $\delta = 0.75$. Solutions to (11) were found numerically.



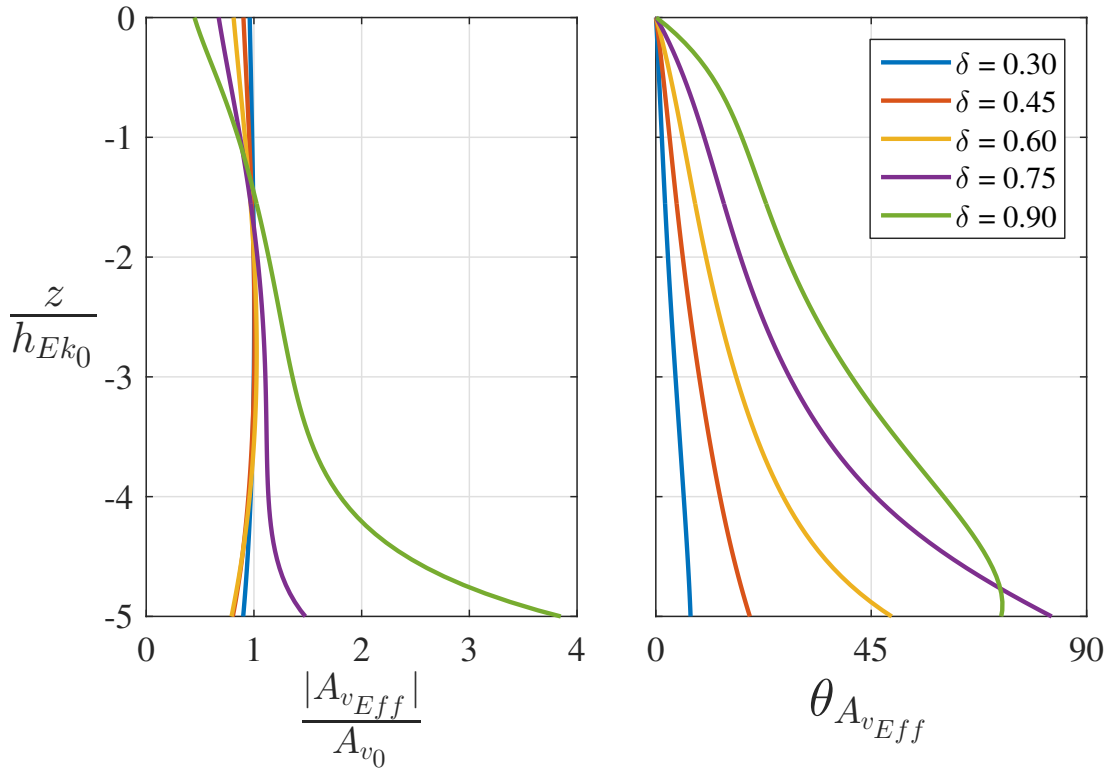
741 FIG. 11. Angle of the time-averaged surface currents relative to the surface wind stress. Negative values
 742 indicate anticyclonic rotation.



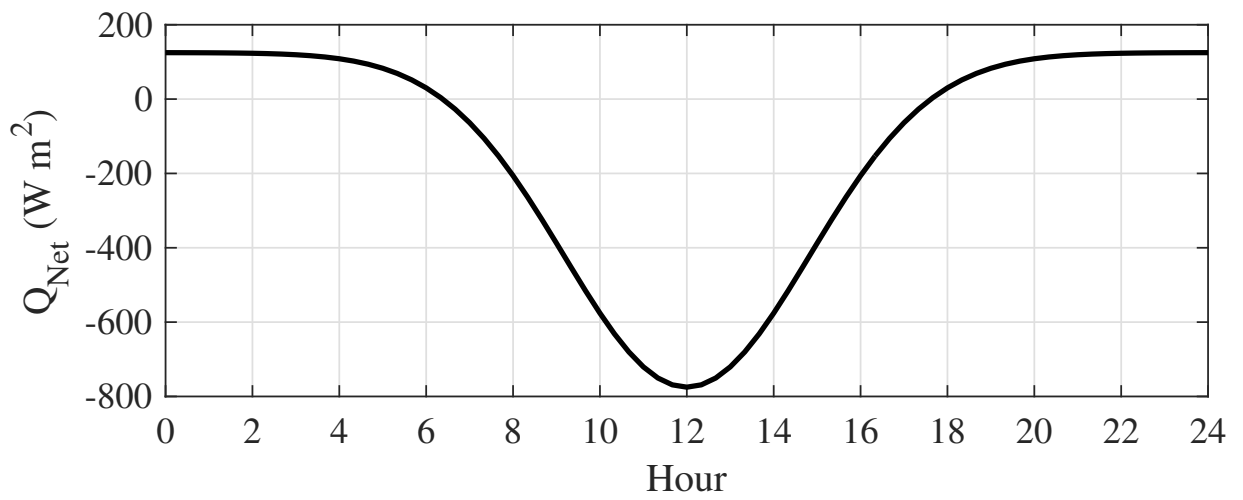
743 FIG. 12. Contour plot of the parameter dependence for the theoretical normalized rectification values, equation
 744 (30), for velocity (left) and shear (right).



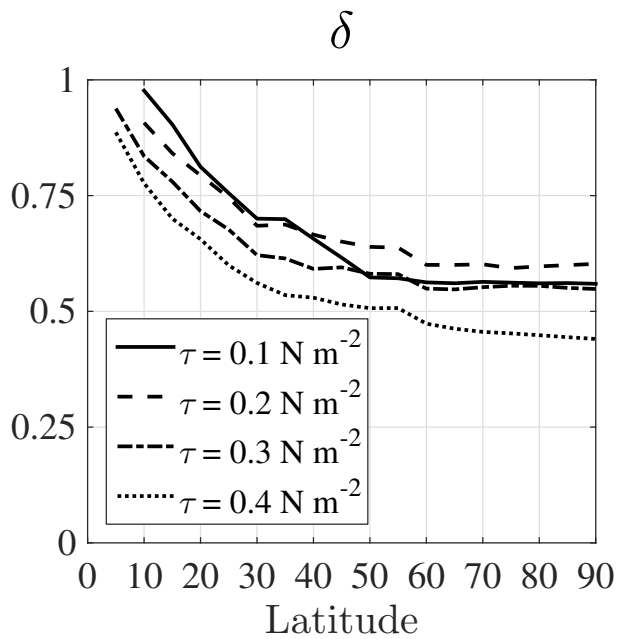
745 FIG. 13. Validation of the rectification implied by the time-periodic solution against a numerical solution of
 746 the initial-boundary-value problem as discussed in section 3c.



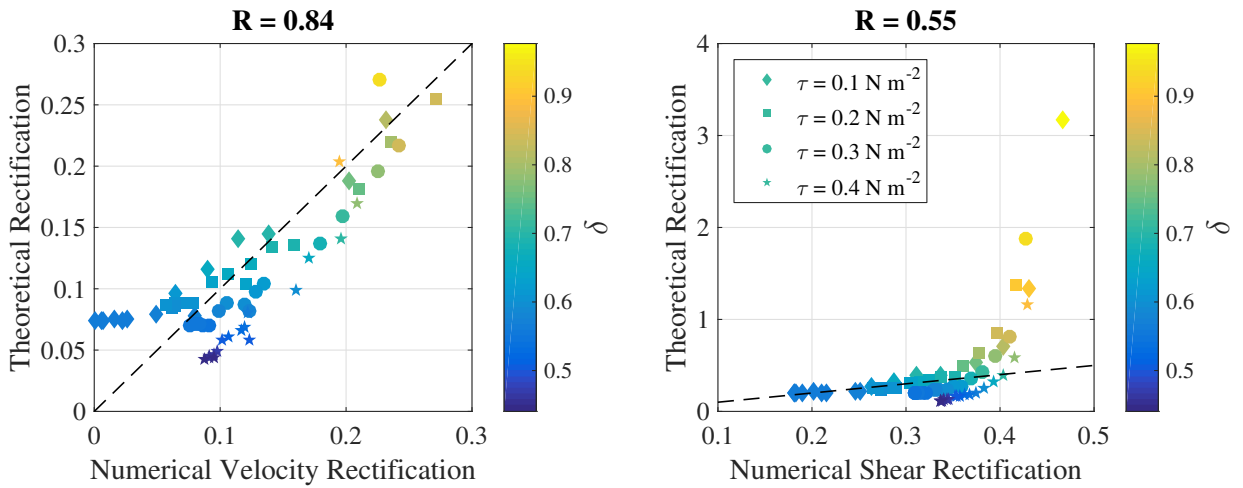
747 FIG. 14. Effective eddy viscosities inferred from the time mean solution for vertically uniform A_v , as defined
 748 by equation (33), with various δ values as shown in the legend. A_{vEff} magnitudes are normalized by the true A_v ,
 749 and angles ($^\circ$) are relative to the local mean-shear direction.



750 FIG. 15. Idealized diurnal cycle of net surface heat flux used to force the numerical model discussed in
751 Appendix A.



752 FIG. 16. Diagnosed magnitude of the diurnal A_v cycle from the numerical model, calculated as described in
 753 Appendix A, as a function of latitude and surface wind-stress (legend).



754 FIG. 17. Comparison of inferred rectification in the numerical model against theoretical predictions for veloc-
 755 ity (left) and shear (right). In each plot, colorscale gives the inferred δ , symbol shape gives the magnitude of the
 756 surface wind-stress as shown in the legend, and the dashed line indicates the 1-1 line. Correlation coefficients
 757 are shown above each plot.